AD-A191 191 NONCONDENSING ROUND TURBULENT GAS JETS IN LIQUIDS(U) 1/1
MICHIGAN UNIV ANN ARBOR DEPT OF AEROSPACE ENGINEERING
E LOTH ET AL. OCT 87 N00014-85-K-0604

UNCLASSIFIED F/G 20/4 NL

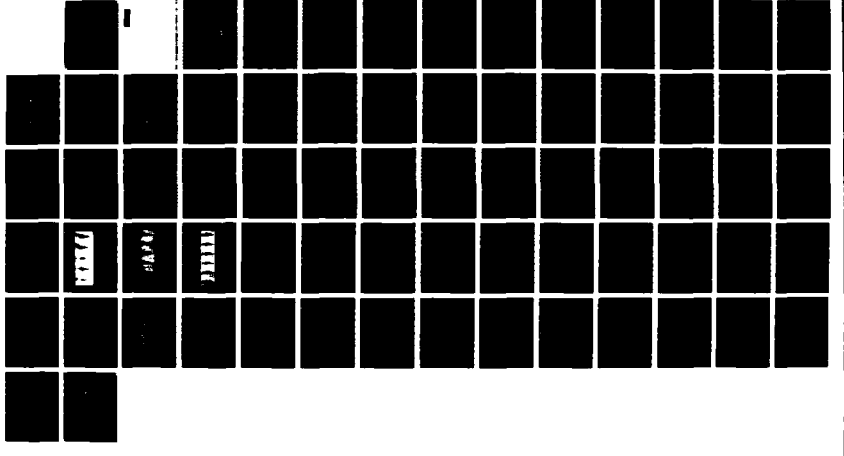

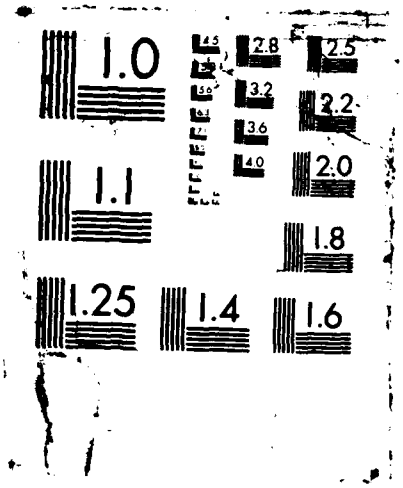
1.0
1.1
1.25
1.4
1.6
1.8
2.0
2.2
2.5
2.8
3.2
3.6
4.0

Interim Report

NONCONDENSING ROUND TURBULENT GAS JETS IN LIQUIDS

by

E. Loth and G.M. Faeth
Department of Aerospace Engineering
The University of Michigan
Ann Arbor, Michigan 48109-2140

Prepared for:

Department of the Navy
Officer of Naval Research
Propulsion and Energetics (Code 1132P)
800 N. Quincy Street
Arlington, Virginia 22217-5000

Contract No. N00014-85-0604
G.D. Roy
Scientific Program Officer

October 1987

Unclassified

SECURITY CLASSIFICATION OF THIS PAGE (When Data Entered)

REPORT DOCUMENTATION PAGE		READ INSTRUCTIONS BEFORE COMPLETING FORM
1. REPORT NUMBER	2. GOVT ACCESSION NO.	3. RECIPIENT'S CATALOG NUMBER
4. TITLE (and Subtitle) Noncondensing Round Turbulent Gas Jets in Liquids		5. TYPE OF REPORT & PERIOD COVERED Interim Report 8/1/85 - 9/30/87
		6. PERFORMING ORG. REPORT NUMBER
7. AUTHOR(s) E. Loth and G.M. Faeth		8. CONTRACT OR GRANT NUMBER(s) N00014-85-K-0604
9. PERFORMING ORGANIZATION NAME AND ADDRESS Department of Aerospace Engineering The University of Michigan Ann Arbor, MI 48109-2140		10. PROGRAM ELEMENT, PROJECT, TASK AREA & WORK UNIT NUMBERS Work Unit NR 097-464
11. CONTROLLING OFFICE NAME AND ADDRESS Office of Naval Research 800 North Quincy Street Arlington, VA 22217-5000		12. REPORT DATE October 1987 13. NUMBER OF PAGES 51 + x pp.
14. MONITORING AGENCY NAME & ADDRESS(if different from Controlling Office)		15. SECURITY CLASS. (of this report) Unclassified 15a. DECLASSIFICATION/DOWNGRADING SCHEDULE

16. DISTRIBUTION STATEMENT (of this Report)

Approved for public release; distribution unlimited.

17. DISTRIBUTION STATEMENT (of the abstract entered in Block 20, if different from Report)

18. SUPPLEMENTARY NOTES

19. KEY WORDS (Continue on reverse side if necessary and identify by block number)

Multiphase flow, gas jets in liquids, compressible turbulent jets.

20. ABSTRACT (Continue on reverse side if necessary and identify by block number)

The structure and mixing properties of noncondensing round turbulent air jets in still water was investigated experimentally, considering both subsonic and sonic underexpanded (with underexpanded ratios up to 8:1) jet exit conditions. Measurements included flow visualization, using flash and high-speed motion-picture photography; mean void fraction distributions, using deconvoluted gamma-ray absorption measurements; mean entrainment velocities, using laser-Doppler anemometry; and mean static

DD FORM 1 JAN 73 1473 EDITION OF 1 NOV 65 IS OBSOLETE
S/N 0102-LF-014-6601

Unclassified
SECURITY CLASSIFICATION OF THIS PAGE (When Data Entered)

pressures along the axis, using a static pressure probe. Analysis was also undertaken to help interpret the measurements, based on the locally-homogeneous-flow approximation (relative velocity differences between the phases neglected) and an effective-adapted-jet approximation for treating the mixing properties of the underexpanded jets.

The static pressure measurements showed the presence of shock-wave containing external expansion region for underexpanded air jets in water, similar to underexpanded air jets in air. The main difference for injection in water is that the external expansion region decays more rapidly. Increasing underexpansion ratios tended to reduce effects of unsteadiness, represented by pressure fluctuations in the flow passage, however, this also increased the extent of the external expansion region and reduced mixing levels along the flow axis. The use of the locally-homogeneous-flow and effective-adapted-jet approximations yielded encouraging predictions, particularly for high underexpansion ratios where effects of flow unsteadiness are reduced. In the fully-developed portion of the flow, the flows exhibited half-widths based on void fraction which were 2-3 times larger than comparable widths in single-phase jets. This behavior was explained by predictions, as a result of the strong sensitivity of void fraction to mixing levels, due to the large density ratio of the flow.

TABLE OF CONTENTS

ACKNOWLEDGEMENTS

The authors wish to acknowledge the assistance of the staff of the Gas Dynamics Laboratories of the Department of Aerospace Engineering for assistance with the experiments; especially Roger Glass, Clete Iott, Warren Eaton and Thomas Griffin. The assistance of T.-Y. Sun, now of Parker-Hannifin Corporation of Cleveland, Ohio, during the initial phases of the investigation is also appreciated. We also thank Clete Iott for valuable technical assistance with flow visualization techniques, and Sue Cowles for help in preparing this report.

LIST OF TABLES

LIST OF FIGURES

NOMENCLATURE

a	acceleration of gravity
C_i	constants in turbulence model
C_E	dimensionless entrainment coefficient
d	jet exit diameter
d_e	equivalent jet exit diameter
f	mixture fraction
g	square of mixture fraction fluctuations
k	turbulence kinetic energy
$\dot{m}_o$	passage flow rate
$\dot{m}$	jet mass flow rate
M	Mach number
$\dot{M}_o$	streamwise thrust on passage
p	pressure
$P(f)$	probability density function of mixture fraction
r	radial distance
r_e	characteristic flow width
Re	passage exit Reynolds number
Ri	passage exit Richardson number
Sc	laminar Schmidt number
S_ϕ	source term in governing equations
T	temperature
u	streamwise velocity
v	radial velocity
x	streamwise distance
Y_i	mass fraction of species i
α	void fraction
β_∞	angle between the jet boundary and the axis
γ	specific heat ratio
ε	rate of dissipation of turbulence kinetic energy
μ	laminar viscosity
μ_{eff}	effective viscosity
μ_t	turbulent viscosity
ρ	density
σ_i	turbulent Prandtl/Schmidt number

ϕ	generic property

Subscripts

a	air
c	centerline value
e	effective exit condition
s	sonic-adapted flow
w	water
o	passage exit condition
∞	ambient condition

Superscripts

t	stagnation condition
$(\bar{})$, $(\bar{})'$	time-averaged mean and root-mean-squared fluctuating quantity
$(\tilde{})(\tilde{})''$	Favre-averaged mean and root-mean-squared fluctuating quantity

1. INTRODUCTION

Processes involving turbulent gas jets injected into liquids are encountered in a number of applications, e.g., liquid metal combustors, metal processing, direct-contact condensers, gas dissolution systems, reservoir destratification systems, and nuclear reactor pressure suppression systems, among others. This investigation considers aspects of turbulent noncondensing gas injection into liquids, motivated by these applications. The main objective was to complete new measurements of the structure of the flow. However, predictions were also undertaken, both to help interpret the measurements, and to initiate evaluation of methods for analyzing the process.

Superficially, injection of a gas jet into a liquid appears to be a simple inverse of injection of a liquid into a gas, however, there are fundamental complications for injection of gases into liquids which have no counterparts for injection of liquids into gases. First of all, the large inertia of the liquid in comparison to the gas causes fundamental unsteadiness of gas jets in liquids at low flow rates, involving oscillatory release of the gas and slugging of the liquid into the jet passage. This unsteadiness is accompanied by appreciable fluctuations of static pressures within the jet passage, as well as within the liquid in the region beyond the jet boundaries (Chan, 1974; Kerney et al., 1972). This can cause excessive noise and vibration, as well as potential blockage of the flow passage in some applications involving reaction of the gas with the liquid (Avery & Faeth, 1975). It has been found that unsteadiness and slugging can be controlled by increasing gas flow rates in the passage, leading to frequent operation with underexpanded exit conditions, where the flow is sonic and the static pressure is greater than the pressure of the ambient liquid, at the exit plane of the passage. This leads to complications of the multiphase flow due to the presence of an external expansion region near the passage exit (involving shock wave cells and compressible flow phenomena) where the static pressure decays to the ambient pressure.

The nature of the external expansion region for gas injection into a liquid is unknown, however, some of the features of this flow can be anticipated based on findings for underexpanded sonic jets in gases (Shapiro, 1954; Addy, 1981). Figure 1 is a sketch of the flow field for a weak underexpanded round jet. Expansion to the ambient pressure is initiated by an expansion fan at the periphery of the passage exit, which accelerates the flow to supersonic velocities. The expansion waves reflect as compression waves due to the constant pressure boundary at the edge of the jet, and these waves steepen to form an oblique intersecting shock wave which crosses the axis as a transmitted shock. When the transmitted shock reaches the opposite edge of the flow, the static pressure behind the shock is again too high, and the process repeats itself, resulting in a series of shock cells. The shock cell pattern is modified by a growing mixing layer between the jet and the ambient fluid, which eventually reaches the axis, ending the external expansion process. Beyond this position, the flows becomes a constant-pressure turbulent jet.

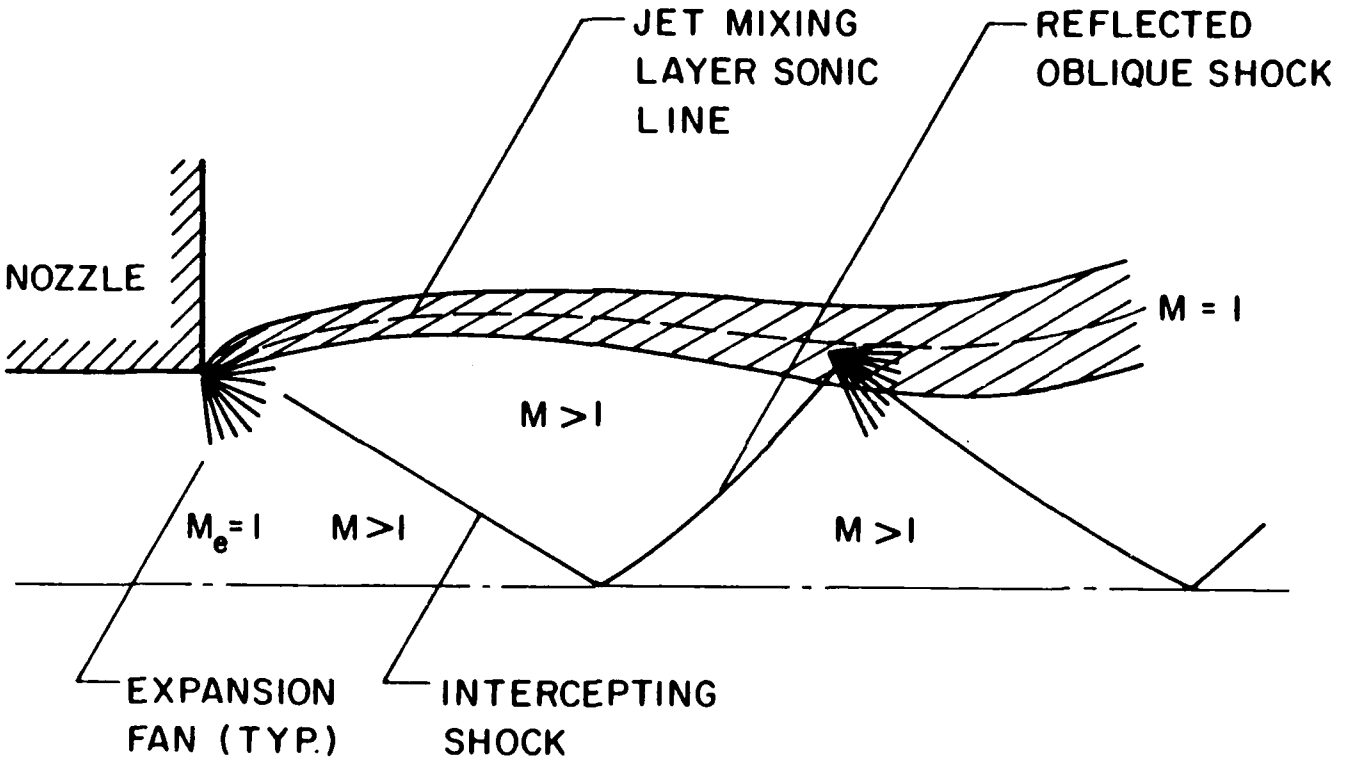

Figure 1. Sketch of weakly underexpanded air jet in still air.

Figure 2 is a sketch of the flow for a strong underexpanded round jet. This flow is generally observed for underexpansion ratios (ratio of the mass flow rate to the sonic mass flow rate) greater than roughly 2 (Addy, 1981). In this case, an oblique transmitted shock is no longer capable of providing a static pressure rise to the ambient pressure at the end of the first shock cell, and a normal shock, called a Mach disk, is formed instead. Subsequent shock cells can involve Mach disks as well, however, the flow eventually evolves to oblique-shock cells and finally a constant-pressure turbulent jet. The presence of a Mach disk introduces a triple point, where the three shocks merge. Since flow through two oblique shocks, and through the Mach disk, does not yield the same velocity, a Mach disk shear layer forms which introduces a Mach disk mixing layer within the core of the flow. Thus, aside from the different shock wave pattern, effects of turbulent mixing are also fundamentally different for weak and strong underexpansion processes.

Based on the findings for gas injection into gases, the flow of a strong underexpanded round jet injected into a liquid is sketched in Fig. 3. Although mixing of gases in liquids differs appreciably from mixing of gases in gases, it can be anticipated that the initial phases of the external expansion process is similar for both flows. Thus a series of shock cells, including Mach disks at higher underexpansion ratios, should be present in the core of the flow near the passage exit. The mixing layer near the edge of the flow, however, involves multiphase flow, with regions having drops in a continuous gas evolving to bubbles in a continuous liquid as the ambient liquid is approached. The growth of this mixing layer, as well as any embedded Mach disk shear layers, eventually ends the external expansion process so that the flow becomes a constant-pressure multiphase turbulent jet.

In view of the complexities of unsteadiness at low flow rates, and the presence of the external expansion region at high flow rates, current understanding of gas injection into liquids is not very complete. Nevertheless, the flow has received some attention in the past which suggests a theoretical approach to gaining a better understanding of the process. Recent work along these lines, from both this laboratory and elsewhere, is briefly considered in the following.

Several studies of gas jets in liquids have been completed in this laboratory, including: noncondensing gas jets in liquids (Tross, 1974; Sun & Faeth, 1986; and Sun et al., 1985), condensing gas jets in liquids (Kerney et al., 1972; Weimer et al., 1973; and Chen & Faeth, 1982), and reacting gas jets in liquids (Avery & Faeth, 1975; and Chen & Faeth, 1983). The earliest experimental studies were confined to gross parameters like the length of the vapor or gas containing region of condensing or reacting jets (Kerney et al., 1972; Weimer et al., 1973; and Avery & Faeth, 1975). As noted earlier, subsonic jet exit conditions yielded unstable flows, with liquid slugging into the injector passage; therefore, these measurements were generally confined to underexpanded jets. Analysis was also undertaken, based on an integral model of turbulence and the locally-homogeneous flow (LHF) approximation, which is widely used to analyze multiphase flows (Soo, 1967; and

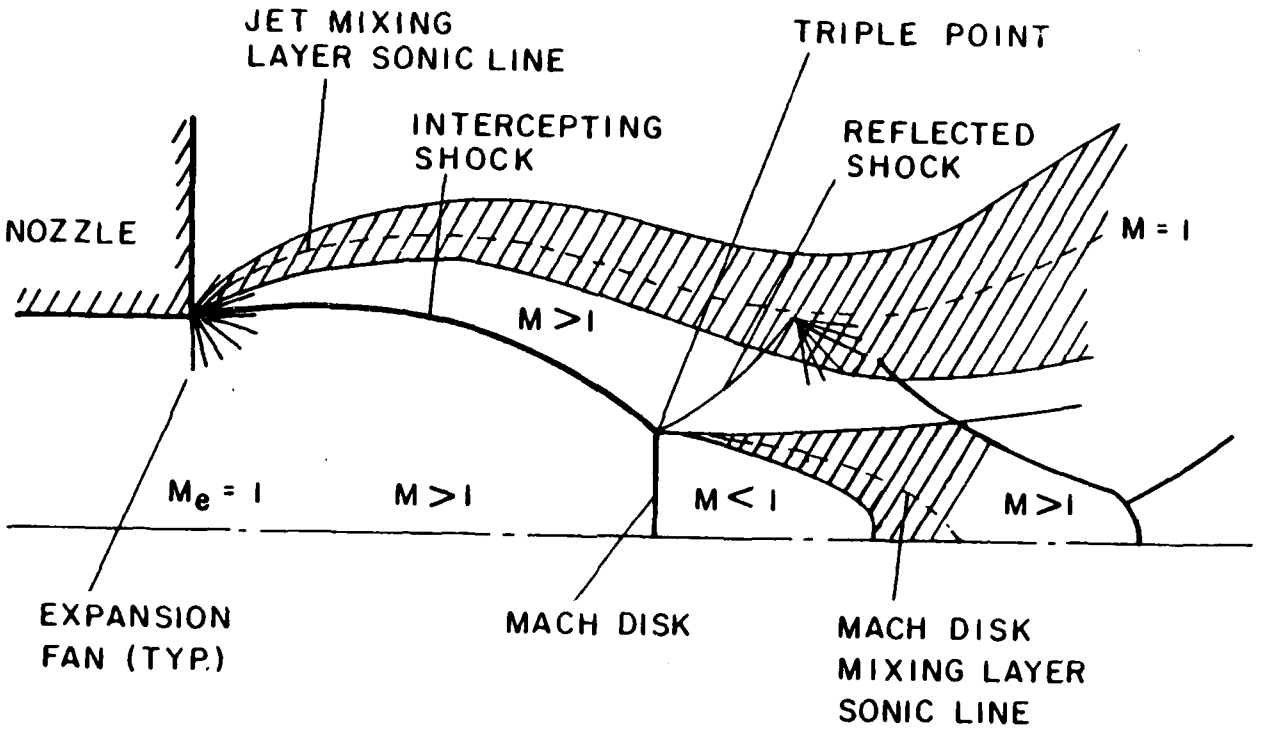

Figure 2. Sketch of strongly underexpanded air jet in still air.

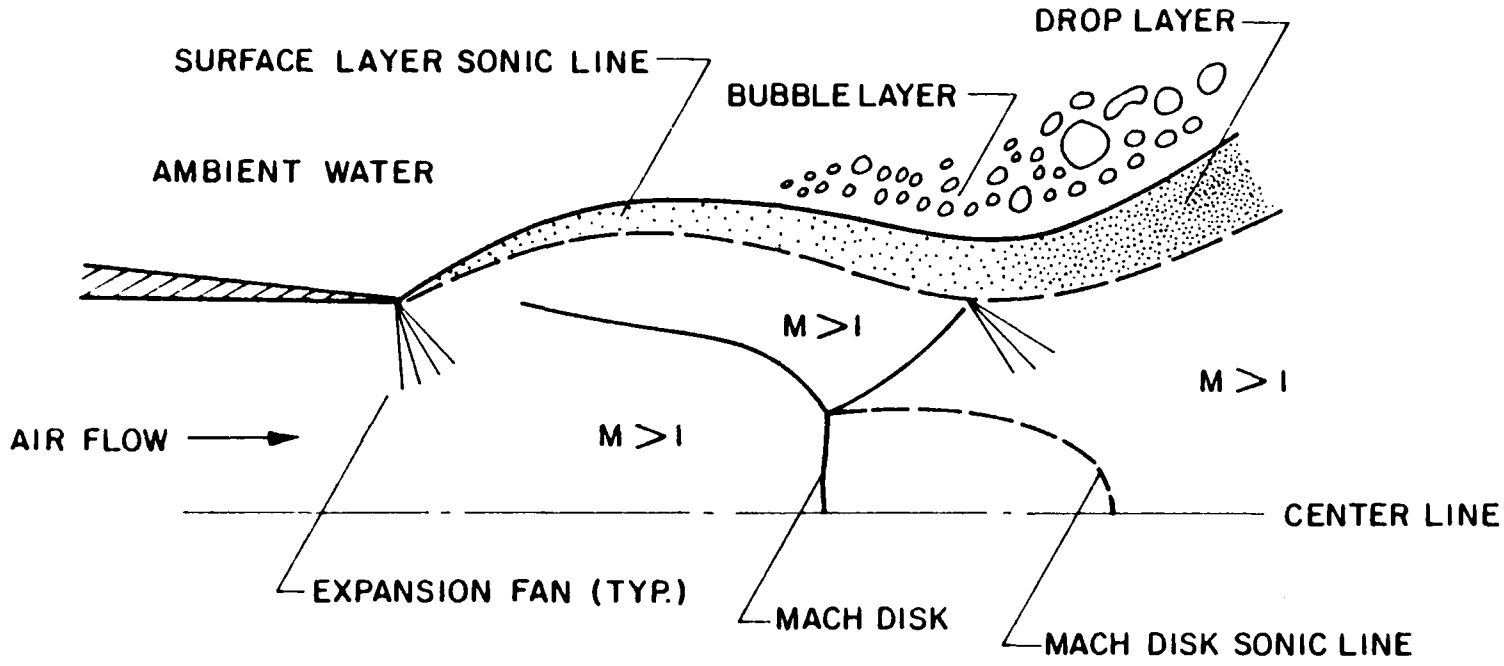

Figure 3. Sketch of strongly underexpanded air jet in still water.

Wallis, 1969). The LHF approximation implies infinitely-fast interphase transport rates and local thermodynamic equilibrium between the phases, i.e., velocity differences (slip) between the phases are neglected and phase and chemical equilibrium are maintained at each point within the flow. The complexities of the external expansion process were treated by defining equivalent adapted jet (static pressure at passage exit the same as the ambient pressure) exit conditions. This approach was reasonably successful for correlating the length of the vapor- or gas-containing region of condensing jets (Kerney et al., 1972; Weimer et al., 1973; and Avery & Faeth, 1975).

Tross (1974), working in this laboratory, considered the structure of adapted and underexpanded air jets injected into still water. Structure measurements were limited to mean void fractions, using an electrical conductivity probe, with predictions based on the LHF approximation in conjunction with an integral model of the turbulence. The reliability of the probe measurements was not very good, due to difficulties of bubbles sliding around the probe when flow velocities are low, and problems of the interaction of surface tension with the probe at all conditions. Similarly, predictions were not very successful, particularly with respect to estimates of flow width (Tross, 1974).

Integral models do not provide a very satisfying picture of flow structure and have little potential for rationally treating the external expansion region; therefore, the next stage of the work involved development of a higher-order turbulence model of the process (Chen & Faeth, 1982, 1983). The conserved-scalar formalism of Bilger (1976) and Lockwood & Naguib (1975) was used, which had provided a successful treatment of constant density, variable density, and combusting turbulent jets during other work in this laboratory (Jeng & Faeth, 1984, Shearer et al., 1979). The LHF approximation was used for this analysis, while only nearly-adapted jet exit conditions were considered to avoid problems of external expansion. A key feature of the combined use of the LHF and conserved-scalar approximations is that scalar properties (void fraction, density, etc.) are only functions of the mixture fraction (the fraction of mass at a point which originated from the injector). These functions, called state relationships, can be found from straightforward adiabatic mixing or adiabatic reaction calculations, typical of fundamental thermodynamic theory. Use of the turbulence model and LHF approximations was successful for predicting the length of the vapor- or gas-containing region of both condensing and reacting jets, with all empirical parameters of the turbulence model fixed at values appropriate for constant-density single-phase jets (Chen & Faeth, 1982, 1983).

Subsequent work in this laboratory involved analysis and measurements of dilute bubbly jets with nearly uniform sized bubbles in the flow at the passage exit (Sun & Faeth, 1986; Sun et al., 1986). The objective was to better understand the limitations of the LHF approximation and to begin development of separated-flow methods at a limit where the topography of the flow (more-or-less round bubbles in a continuous liquid) was known. Measurements included phase velocities, using laser Doppler anemometry (LDA); void volumes and bubble sizes, using flash photography; and bubble number fluxes, using Mie

scattering. In addition to LHF predictions, two separated flow analyses were considered, as follows: (1) a deterministic separated flow (DSF) approach, which allowed for finite interphase transport rates but ignored bubble/turbulence interactions; and (2) a stochastic separated flow (SSF) approach, which allowed for both finite interphase transport rates and bubble/turbulence interactions by random-walk (Monte Carlo) computations of bubble motion and transport (bubble life histories). Comparisons between predictions and measurements showed that the LHF approximation was reasonably good near the passage exit, where maximum relative velocities between the phases are small in comparison to mean flow velocities. The SSF approach was successful throughout the flow, particularly for predicting the evolution of void fraction distributions from near-injector conditions, where effects of relative velocities are small, to conditions far from the injector, where effects of finite interphase transport rates begin to dominate the mixing process. In contrast, the DSF approach was not effective at any point in the flow.

Related studies by other workers tend to parallel activities in this laboratory. Structure measurements for gas jets in liquids are very limited due to experimental difficulties for high void fraction multiphase flows. Earliest work by Cumo et al. (1978), Kudo et al. (1974), Lee et al. (1979) and Young et al. (1974) involved measurements of only the gross features of condensing jets, like the length of the vapor-containing region. Relevant portions of this data were used to evaluate LHF analysis of condensing jets (Chen & Faeth, 1982). Bakaklevskii & Chekhovich (1978) report temperature and dynamic pressure profiles in condensing plane jets in coflow, however, measurement accuracy and flow conditions are too uncertain to provide more than a rough guide to structure. Chan (1974), Chun & Sonin (1984), Lambier & Chow (1984) and Simpson & Chan (1982) measured static pressures near the passage exit for subsonic condensing jets, finding the large pressure pulsations indicative of unsteady flow that were mentioned earlier. Structure measurements are more numerous for noncondensing jets, but these results either involve the use of probes, or are limited to dilute bubbly flows far from the passage exit (Abdel-Aal et al., 1966; Mahalingen et al., 1976; Ohba et al., 1977; and Ohba, 1979).

Study of the near-field region of underexpanded gas jets in liquids has been very limited. Several workers have pointed out the increased stability of underexpanded jets, as noted earlier (Kerney et al., 1972; Weimer et al., 1973). However, proof of even the existence of a shock wave containing region, much less its role in stabilizing the flow, has not been reported. Approximation of the external expansion region as an effective adapted jet for the purposes of estimating mixing properties has been proposed, but assessment of this approach has been very limited (Kerney et al., 1972; Weimer et al., 1973). In contrast, there is substantial information available concerning the structure and mixing properties of underexpanded gas jets in gases, see Chuech et al. (1987, 1988) for a review of past work in this area and recent measurements and predictions for these flows.

In summary, existing measurements of the structure of gas jets in liquids is very limited, particularly for the high void fraction region near the passage exit. Use of the LHF

approximation has yielded promising results, for gross quantities like the length of condensing jets, however, the capabilities of this approach for predicting structure have not been adequately assessed since pertinent data are not available. Finally, effects of external expansion, which are important for practical systems involving gas injection into liquids, are poorly understood.

The objective of the present investigation was to begin more detailed study of turbulent gas jets in liquids, emphasizing processes in the high void fraction, near-injector region. Attention was limited to round air jets in still water, where momentum exchange is the only relevant interphase transport process. New measurements were completed for both subsonic and underexpanded jets, as follows: flow visualization, using flash and motion picture photography; static pressures along the axis, using a static-pressure probe; mean void fraction distributions, using gamma-ray absorption; and jet entrainment rates as well as jet exit conditions, using laser-Doppler anemometry. Predictions of flow properties were also completed, to help interpret the measurements and to initiate evaluation of methods for estimating flow properties. These considerations were limited to use of the LHF approximation and a simplified higher-order turbulence model, similar to Chen & Faeth (1982, 1983), except for extension to use a Favre-averaged formulation which simplifies approximations concerning density fluctuations (Bilger, 1976). Furthermore, no attempt was made to deal with the complexities of a multiphase shock wave containing external expansion process; rather, present calculations were limited to the use of effective adapted jet approximations for underexpanded jets.

The report begins with consideration of experimental and theoretical methods. Results are then considered, treating flow definition (properties of the flow passage and flow visualization) and flow structure, in turn.

2. EXPERIMENTAL METHODS

2.1 Test Apparatus

Figure 4 is a sketch of the test apparatus. The arrangement consists of a large water-filled tank, a traversable injector assembly, and instrumentation for nonintrusive velocity (LDA) and void fraction (gamma-ray absorption) measurements. The water-filled tank was 1 m × 2 m × 2 m high. The tank was open at the top and had windows covering the full height of the four sides. This provided a reasonable simulation of a stagnant bath and flexibility of optical access for flow visualization and optical diagnostics. The injector flow created a significant disturbance at the liquid surface, with the formation of a large-scale wave that traversed the tank from side to side. This was controlled by the installation of wave suppressors near the surface (not shown in Fig. 1). The wave suppressors consisted of two 400 mm wide plates, at an angle of 30° from the horizontal, which ran the full length of the tank along each side, submerged half-way in the water. The suppressors provided an artificial beach which reduced surface disturbances to acceptable levels (wave heights of less than 75 mm which yielded pressure disturbances less than 2 kPa at the passage exit, according to deep wave theory).

The injector was mounted on a U frame traversing system and injected vertically upward. The traversing system provided vertical traverses with a manual clamp arrangement having a positioning accuracy of 2 mm; and a manual trim adjustment along the short side of the tank also having a 2 mm positioning accuracy. Major traverses were in the horizontal direction along the long side of the tank. This was accomplished by mounting the injector frame on a linear bearing system motor controlled Unislide Assembly (Velmex Model 8300) which was controlled by a microcomputer. This arrangement had a positioning accuracy of 0.1 mm. The U-frame injector support was designed to keep all components outside of the jet flow region (the distance between vertical supports was 750 mm with the injector mounted half-way between the vertical supports).

The air supply was drawn from the laboratory facilities, consisting of dried and filtered air (dew point less than 240K) in a storage tank at pressures up to 15 MPa. Air flow rates were controlled with pressure regulators and metered with critical flow nozzles (Flow Engineering Co., calibrated to 0.1 percent accuracy). Pressures on the upstream side of the critical flow orifice were measured with a 250 mm diameter Heise pressure gage (0-2 MPa range). The air leaving the test tank was simply vented into the laboratory since the arrangement was located in a well-ventilated high-bay area (30 m × 60 m × 15 m high).

Figure 5 is an illustration of a typical injector assembly. The air flow enters a plenum and then passes through a honeycomb flow straightener having a 1.6 mm cell width and a length of 30 mm. After a short calming section, having a diameter of 32 mm, the flow passes through an axisymmetric converging section to the constant area injector passage. Two injector passages were used, having inside diameters of 4.9 and 11.0 mm and lengths of 233 mm; as a result, the flow at the exit of the passage approximated fully-

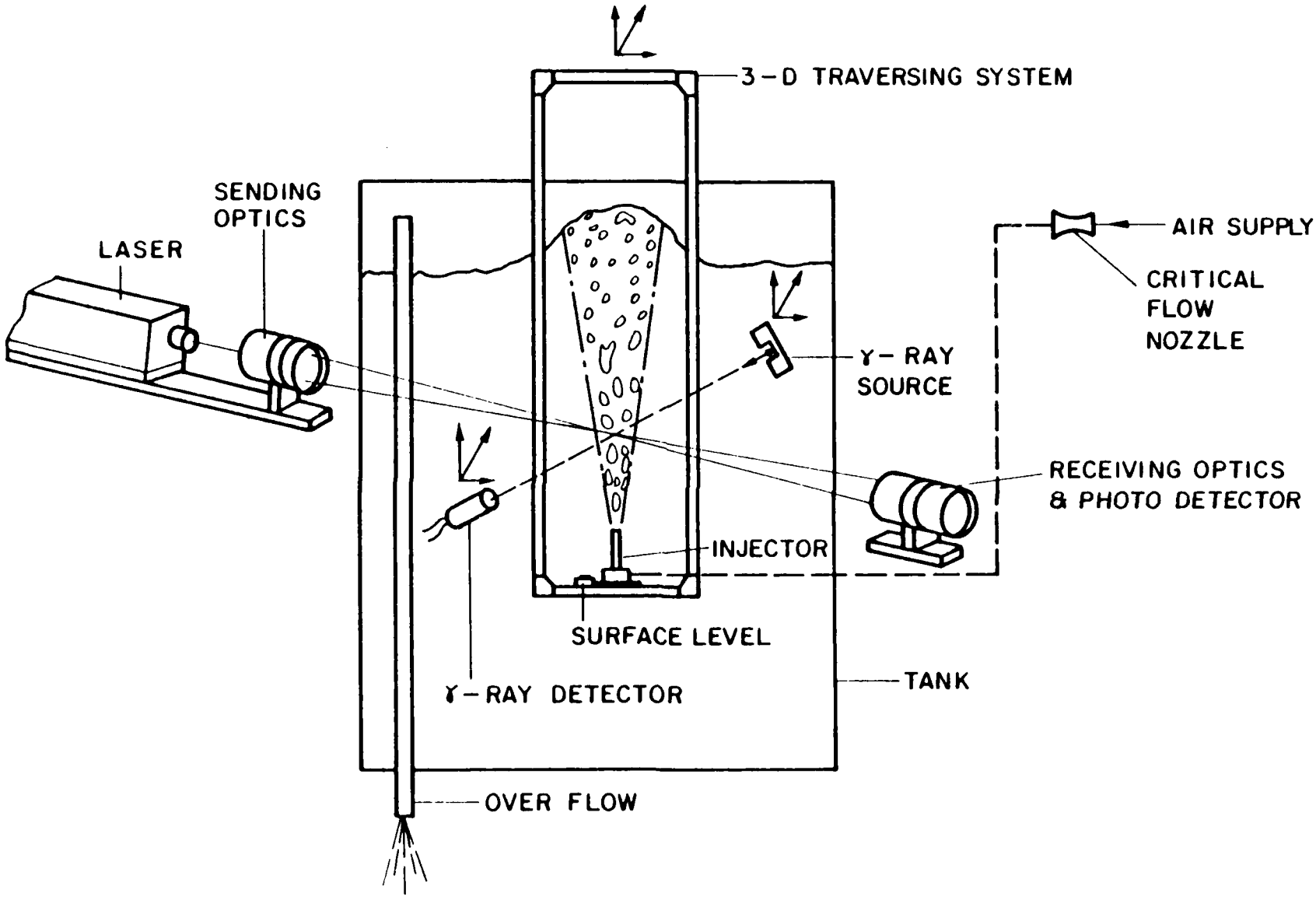

Figure 4. Sketch of test apparatus.

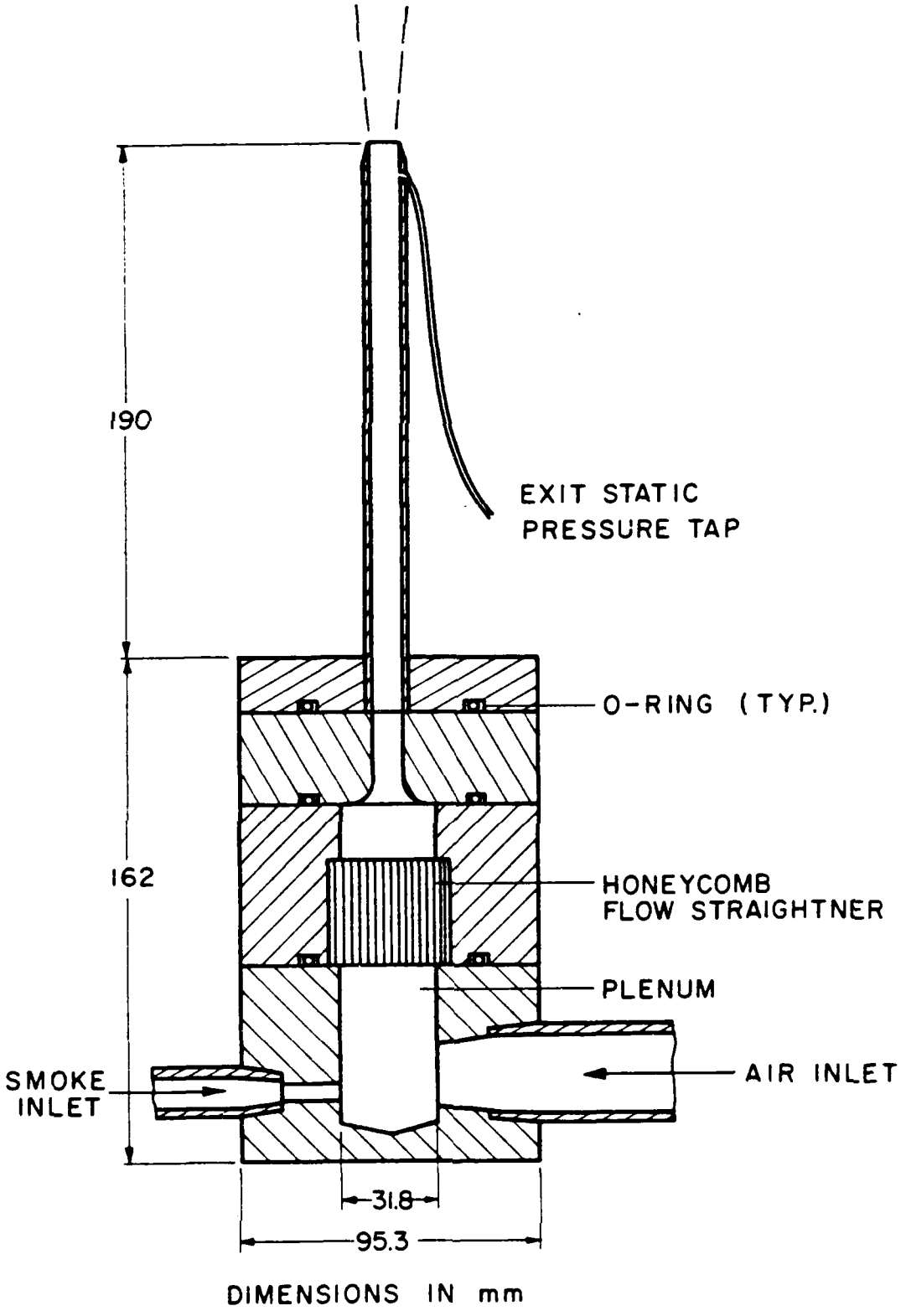

Figure 5. Sketch of injector.

developed pipe flow. A static pressure tap, located one diameter upstream from the injector exit, was used to find the static pressure at the end of the injector. A port in the plenum chamber was also monitored to study the transient pressure variations in the plenum.

2.2 Instrumentation

Flow Visualization. Flash photographs were obtained in the near-injector region. The flow was illuminated using a Xenon Corp. Model 457B, Pulsar Flashlamp system, yielding up to 10 J/pulse with a flash duration of roughly 1 μs, positioned near the camera. The photographs were obtained with an open camera shutter within a darkened room; therefore, the time of exposure was controlled by the duration of the flash, which was short enough to stop the motion for present test conditions. The camera was located roughly 200 mm from the glass wall of the tank, with the jet positioned at the center of the tank. A Graflex Sychromatic Camera with a 25 mm wide-angle lens (F1.8), was used in conjunction with Polaroid Type 57 (ASA 3200) black and white film.

Motion picture photographs were also taken of the flow, using continuous illumination from positions near the camera. These were obtained with a Redlakes Hycam high-speed camera operating at speeds of roughly 1000 pictures/s. The camera was located in the same position as the camera for flash photographs, and was also fitted with a 25 mm focal length (F1.8) lens. Kodak, 4-X, negative film (ASA 400) was used for these photographs.

Static Pressures. Static pressures were measured along the axis of the jet, for a passage diameter of 11.0 mm, using a probe system similar to that used by Eggers (1966) for underexpanded air jets in air. The arrangement is illustrated in Fig. 6. The static pressure probe consisted of a 1 mm diameter stainless-steel tube with the upstream end closed and a 0.4 mm diameter pressure tap located so that it could be traversed to cover the region $-1 \leq x/d \leq 7$. The probe was centered along the axis by two supports: one located within the flow passage, roughly 6 diameters from its downstream end; the other located in the bath, roughly 13 diameters from the passage exit. The downstream mount had a set screw, which allowed the static tap to be firmly positioned (within 0.1 mm) at various distances from the passage exit. A capillary purge system, in the line to the pressure gage, provided a means of purging the probe of liquid during operation with air/water jets.

Static pressures were read with a 250 mm diameter Heisse pressure gage (0-2 MPa, system, to provide reasonable measuring accuracy of the full range of experimental conditions. The experimental uncertainties of the static pressure measurements (95 percent confidence) are estimated to be less than 30 percent of the pressure difference between the jet and the water bath.

Void Fractions. Distributions of time-averaged void fractions were measured using gamma-ray absorption. Absorption measurements for several cord-like paths through the flow, at a particular streamwise distance, were deconvoluted to find radial distributions of

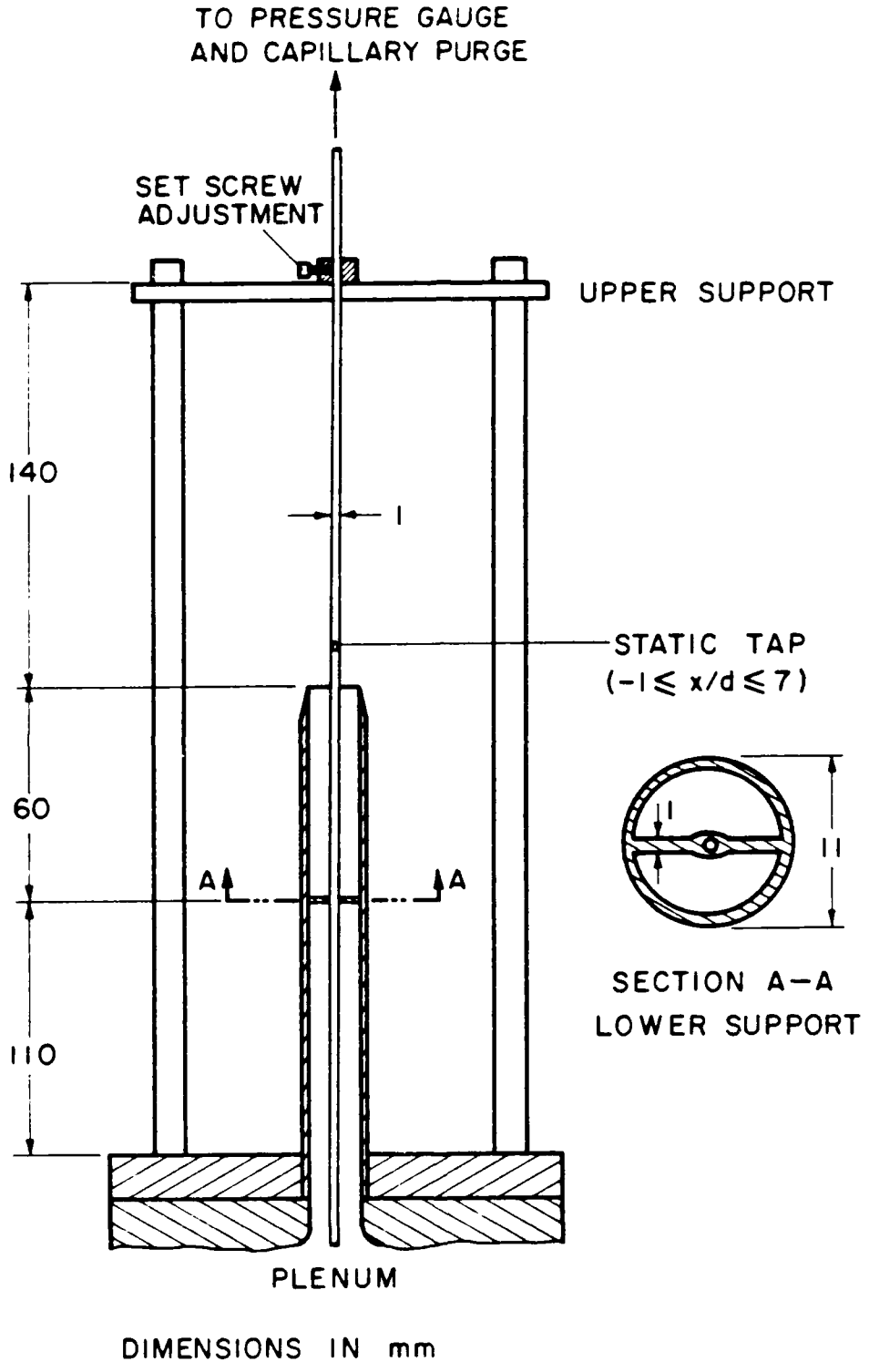

Figure 6. Sketch of static pressure probe.

time-averaged void fraction. The arrangement of the gamma-ray absorption system is sketched in Fig. 7.

Gamma-rays were obtained from a Co-57 source (Amersham Inc., 2 mCi, 271 day half-life). The source was placed in a lead casket, with an output beam of gamma-rays directed across the flow using a lead collimator (2 mm diameter and 13 mm long). After traversing the flow, the beam passed through a lead aperture (2, 3, and 5 mm diameter, depending on the jet width, and 13 mm long) to the detector (EG & G Model 905-1 sodium iodide scintillator and photomultiplier). The detector signal was preamplified and then processed by an EG& G Model 590 A single-channel analyzer and amplifier, and an EG & G Model 974 timer/counter. The output counts of the timer/counter were then collected and stored, for various sampling times, using an IBM-AT computer.

A typical energy spectrum from the Co-57 gamma-ray source, obtained using the present detector system, is illustrated in Fig. 8. The maximum count rate is associated with the 122 keV gamma-ray emission of the Co-57 source, which is broadened due to the limited resolution of the detector. Other peaks appearing on the spectrum include k-β X-ray emission from lead at roughly 90 keV and gamma-ray emission from Co-57 at 136 keV. The absorption window for the present measurements is also shown in Fig. 8, ranging from 114-128 keV. This window was effective for reducing effects of background radiation while yielding reasonable count ratio for the measurements.

At each axial position, absorption measurements were accumulated at 20-40 cord like paths through the flow, acquiring roughly 10,000 counts at each position. The linear absorption coefficient of gamma-rays for air is about four orders of magnitude smaller than for water; therefore, the logarithm of the counting rate is proportional to the fraction of air in the radiation path. Assuming axisymmetric flow, the absorption measurements were deconvoluted, following Santoro et al. (1981), to obtain radial profiles of time-averaged void fraction.

The accuracy of the deconvolution procedure is influenced by the relative change in the count rates for each cord-like path; therefore, the source and detector were located near the edge of the flow, with both units submerged in the water bath. This was done by enclosing them in plexiglass housings, with wiring passing to the surface of the bath through flexible plastic tubing. The photomultiplier requires high voltages, ca. 1 kV; therefore, it was important to prevent possible water leakage to this component. This was accomplished by maintaining an excess air pressure within the housing so that any leaks could be seen immediately by a stream of air bubbles eminating from the leak.

Bias errors in the void fraction measurements are influenced by whether liquid laminae in the absorption path are parallel or normal to the path (Ohba, 1979; Schrock, 1969). Low intensity ratios reduced uncertainties due to this effect to less than 5 percent, based on the findings of Ohba (1979). Dynamic bias errors, due to turbulent fluctuations

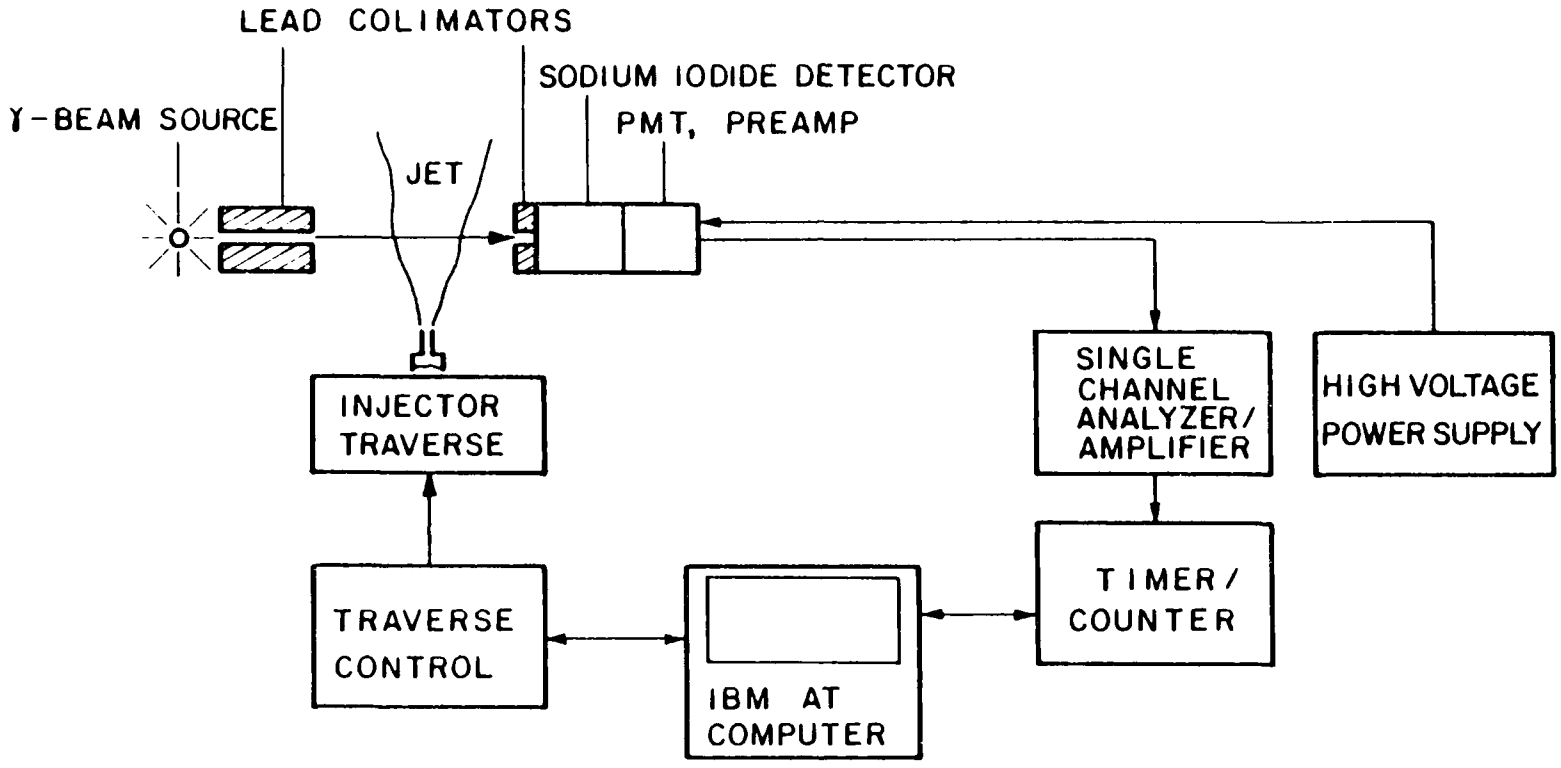

Figure 7. Sketch of gamma-ray absorption system.

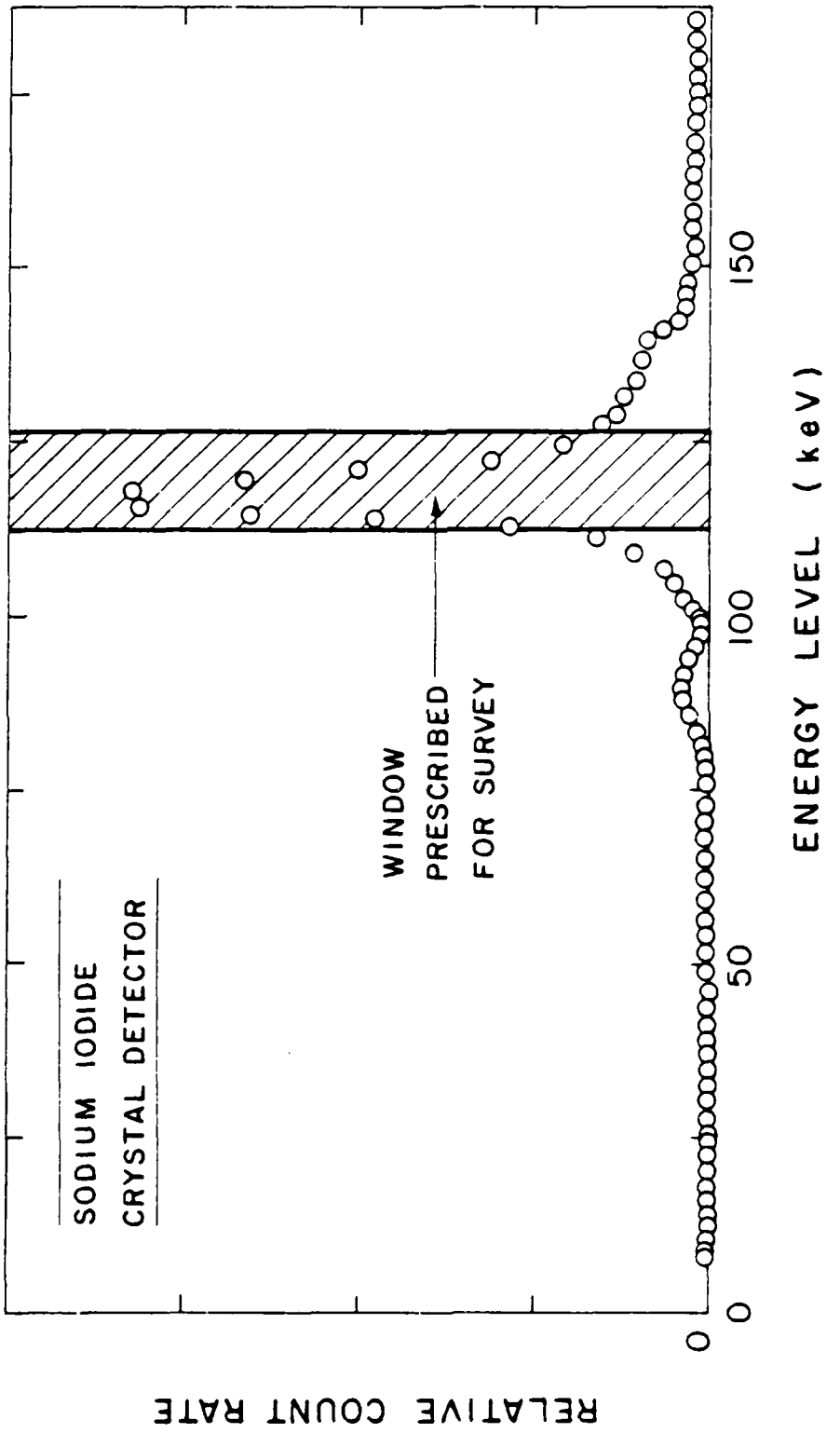

Figure 8. Energy spectra of Co-57 source from NaI detector.

of void fraction along the path were estimated by deconvolutions through a linearized error analysis, which showed a bias error of less than 5 percent.

The main source of experimental uncertainty was amplification of count rate uncertainty during the implementation of the deconvolution process. This was calculated using the matrix model given by Limbaugh & Kneile (1984) for results obtained by deconvolution of data with a prescribed uncertainty. This resulted in experimental uncertainties along the centerline (95 percent confidence) of less than 10 percent, with relative uncertainties increasing inversely proportional to the indicated mean void fraction at off-axis positions. Assessment of errors, based on retrieving a mean void fraction of one for several positions in the jet air core, confirmed uncertainty estimates within these limits.

Velocities. Mean and fluctuating streamwise velocities at the passage exit (to define initial flow conditions) and mean jet entrainment velocities in the liquid, were measured using LDA. For velocity measurement at the passage exit the test tank was drained. Figure 9 is a sketch of the LDA system.

The LDA was based on the 514.5 nm line (TEM_{00} mode) of an argon-ion laser (Coherent, INNOVA 90-4) operated at 0.6 watts. A dual-beam forward-scatter arrangement was used, with Bragg-cell frequency shifting (40 MHz with electronic downshifting to convenient output frequency ranges, TSI Model 9182-12) to control directional bias and ambiguity. The beam spacing was 50 mm, with a 600 mm focusing lens. A photomultiplier detector (TSI Model 9162) and burst counter (TSI Model 1990C) were used to collect and process the LDA signals. Low-burst density (low probability of more than one scattering particle in the measuring volume) and high data density (time between validated velocity determinations small in comparison to estimated integral time scales) signals were obtained; therefore, the analog output of the burst counter was time averaged, using a 12 bit Le Croy Model 8212 A/8, A/D converter, four Le Croy Model 8800A 32k memory banks, and an IBM 9002 microcomputer, to yield unbiased time averages.

Other aspects of the LDA differed for measurements of passage exit velocities and entrainment. Measurements at the passage exit required good spatial resolution, since the flow field was small. This was accomplished using off-axis detection (30°) and 250 mm focal length collecting optics. This provided a cylindrical measuring volume having a diameter of 250 μm and a length of 320 μm. The air flow through the passage was seeded with bayol particles, having diameters of roughly 500 nm, using a generator described by Chuech et al. (1987). The generator added particles to the flow at the plenum chamber of the injector, see Fig. 5. Concentration bias was not a factor for these measurements, since the flow was seeded uniformly; while gradient bias was small due to the small measuring volume; therefore, experimental uncertainties were largely governed by finite sampling times. It is estimated that experimental uncertainties (95 percent confidence) of time-averaged mean and fluctuating streamwise velocities are less than 5 and 20 percent, near the axis of the flow, and inversely proportional to mean velocity levels elsewhere.

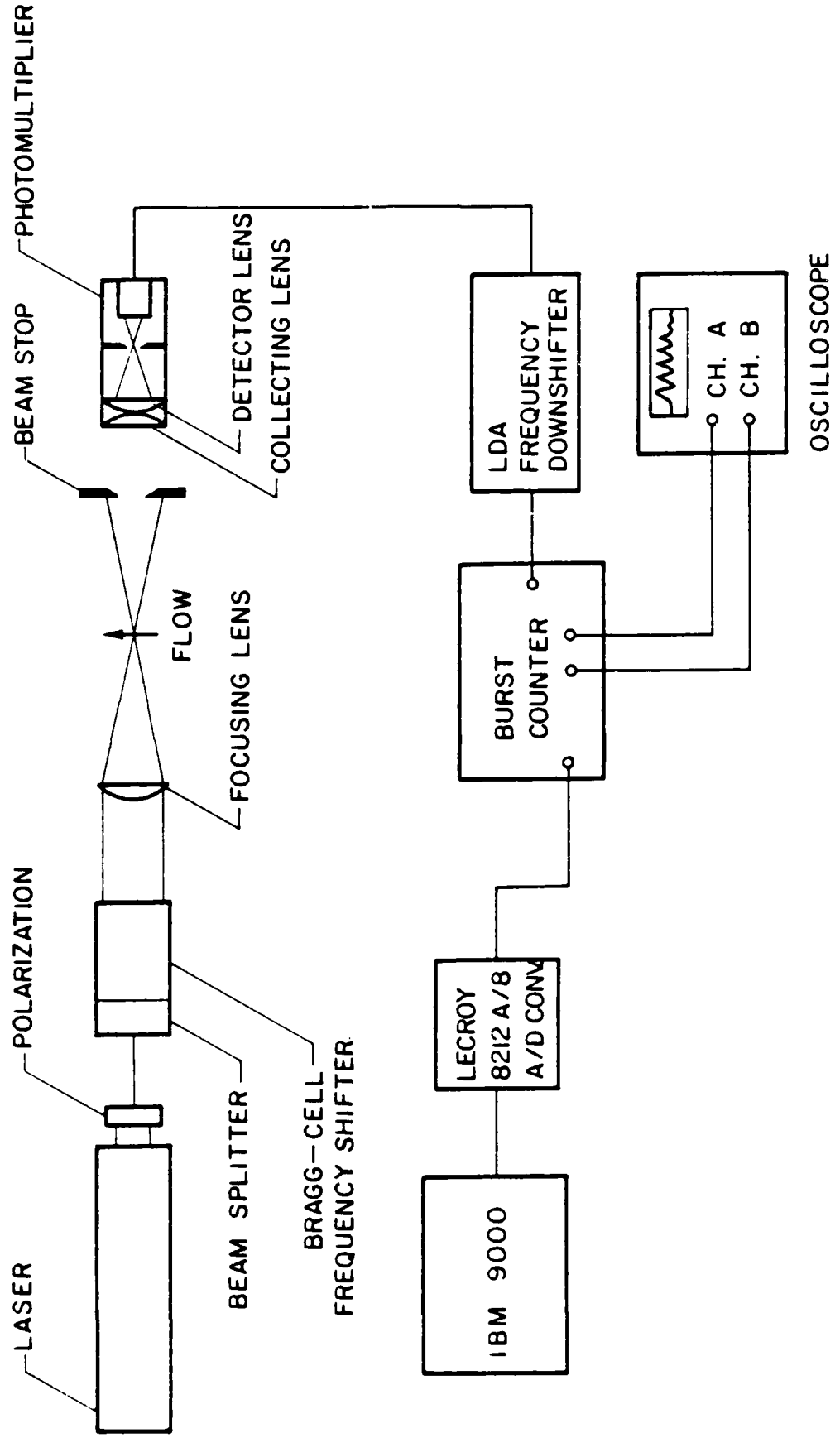

Figure 9. Sketch of LDA system.

The rate of entrainment of the multiphase jet is a useful indicator of their turbulent mixing properties. Furthermore, entrainment is readily accessible for nonintrusive LDA velocity measurements since only the liquid-phase velocities near the edge of the jet must be measured. Due to the extended jet passage used during the present experiments, entrainment velocities were not strictly radial; therefore, both mean radial and streamwise velocities were measured, just outside the two-phase flow region. This was accomplished by using forward-scatter collection with a 600 mm focal length collecting lens. The two velocity components were measured by appropriately orienting the optical plane of the LDA. The 20° off-axis receiving optics provided a cylindrical measuring volume having a diameter of 200 μm and a length of 400 μm, with the long dimension in the tangential direction. The LDA signal was obtained from natural seeding particles in the water. Concentration bias was not a factor, and gradient bias was small, since the long dimension of the measuring volume was tangential; therefore, experimental uncertainties were largely governed by finite sampling times. It is estimated that experimental uncertainties (95 percent confidence) of time-averaged streamwise and radial mean entrainment velocities are both less than 10 percent.

Entrainment. The entrainment concept is appropriate for steady shear flows satisfying the boundary-layer approximations. Formally, the rate of entrainment is equal to the rate of increase of the mass flow rate of a jet with streamwise distance. Thus for axisymmetric flow in a still environment, the entrainment rate becomes:

$$\dot{m}/dx = (d/dx) \int \pi r \rho \bar{u} dr = - \lim_{r \to \infty} (2\pi r \rho v) \qquad (2.1)$$

Present measurements were made along a jet boundry just outside the gas-containing region. Measuring $\tilde{u}_\infty$ and $\tilde{v}_\infty$ at the radial distance of the boundary, r_∞ yields the following expression for the increase of the mass flow rate of the jet, per unit streamwise distance:

$$\dot{m}/dx = 2\pi r_\infty \rho_\infty (u_\infty \tan \beta_\infty - v_\infty) \qquad (2.2)$$

where β_∞ is the angle between the jet boundary and the axis. This yields the following expression for the dimensionless entrainment coefficient:

$$C_e = 2\pi r_\infty \rho_\infty^{1/2} (u_\infty \tan \beta_\infty - v_\infty) / \dot{M}_0^{1/2} \qquad (2.3)$$

where $\dot{M}_0$ is the streamwise thrust on the passage.

Uncertainties in entrainment measurements resulted from uncertainties in the velocity measurements and definition of the edge of the jet. Estimated experimental uncertainties of the entrainment measurements (95 percent confidence) were less than 20 percent.

2.3 Test Conditions

Test conditions are summarized in Table 1. Flow rates varied from subsonic jets to highly underexpanded sonic jets (underexpansion ratios, $\dot{m}/\dot{m}_s$ in the range 0.6-8.0). For $\dot{m}/\dot{m}_s \geq 1$, the ratios of the passage exit to ambient static pressures are equivalent to $\dot{m}/\dot{m}_s$, implying that the tests should include conditions with Mach disks present, if the near-field external expansion region is similar for injection of air into air and into water. Flow Reynolds numbers are quite high, ca. 10^5, with approximately fully developed pipe flow at the passage exit (which will be subsequently shown); therefore, the jets were turbulent. Richardson numbers were relatively low, ca. 10^{-4}; therefore, effects of buoyancy were small in the external expansion region near the passage exit. However, mixing is rapid for air injection into water and the large density difference between water and air causes significant effects of buoyancy farther downstream, $x/d > 20$.

Table 1 Summary of Test Conditions

$\dot{m}/\dot{m}_s$[a]	ρ_o (kg/m^3)	T_o[t](K)[b]	$\dot{m}_o$(g/s)[c]	$\dot{M}_o$(N)	Re/10^5 [d]	Ri/10^{-4} [e]
4.9 mm injector:						
0.6	1.36	297.1	5.28	1.11	0.80	8.14
1.0	1.52	296.0	8.68	2.73	1.34	3.31
2.0	3.06	294.9	17.5	7.42	3.62	1.21
4.0	6.12	294.4	35.8	16.7	8.01	0.54
8.0	12.3	293.7	71.7	35.9	17.2	0.25
11.0 mm injector:						
0.6	1.36	297.1	26.3	5.53	1.80	18.5
1.0	1.52	296.0	43.8	13.8	3.01	7.41
2.0	3.06	294.9	87.7	37.3	8.16	2.73
4.0	6.12	294.4	174.0	83.6	18.5	1.22

Ambient water: $T_\infty = 294K \pm 2K$, $p_\infty = 107.5$ kPa $\pm$ 0.7 kPa.

[a]2.1% standard deviation in choked mass flow ratio.

[b]1.0% standard deviation

[c]1.9% standard deviation

[d]$Re = \rho_o \dot{M}_o d/(\mu_o \dot{m}_o)$

[e]$Ri = (\rho_\infty / \rho_o - 1)\, ad\, (\dot{m}_o / \dot{M}_o)^2$

3. THEORETICAL METHODS

3.1 General Description

Theoretical considerations were limited to steady (in the mean) adapted flow, i.e., static pressure at the passage exit equal to the ambient pressure. Thus, underexpanded jets were approximated using effective adapted-jet exit conditions, following an approach suggested by Kerney et al. (1972). In other respects, the analysis follows the conserved-scalar formalism under the LHF approximation, similar to Chen & Faeth (1982, 1983) but is extended to use mass-weighted (Favre) averages instead of time averages, in order to eliminate numerous terms involving density fluctuations, as recommended by Bilger (1976). Turbulent mixing is represented by a simplified k-ε-g turbulence model, similar to an early recommendation of Lockwood & Naguib (1975). However, specific empirical constants using the Favre-averaged formulation were taken from Jeng & Faeth (1984): these values were successfully calibrated for a variety of constant and variable density single-phase jets. Furthermore, the approach has also successfully treated effects of different states at the passage exit; specifically at the limits of fully-developed pipe flow and slug flow (Jeng & Faeth, 1984; Shuen et al., 1984; Chuech et al., 1987, 1988).

The major assumptions of the analysis are as follows: steady (in the mean) axisymmetric turbulent jet with no swirl; the boundary layer approximations apply; locally-homogeneous flow, implying negligible relative velocity between the phases and local thermodynamic equilibrium at each point in the flow; equal exchange coefficients of all species, phases and heat; buoyancy considered in the governing equations for mean quantities, but ignored in the governing equations for turbulence quantities; and effects of mean kinetic energy, viscous dissipation, and compressibility were ignored. The first assumption is a condition of the experiments (at least superficially) while the LHF approximation is the fundamental hypothesis that will be examined by the comparison between predictions and measurements. The other assumptions have been used in the past with some success (Chen & Faeth, 1982, 1983): their justification will be discussed in the following.

The assumption of equal exchange coefficients of all species and heat has been widely used for single-phase flows in the past, and is the fundamental approximation needed to apply the conserved scalar formalism (Lockwood & Naguib, 1975; Bilger, 1976; Jeng & Faeth, 1984). Since Prandtl and Schmidt numbers of gases are near unity, this approximation is reasonable even at low Reynolds numbers where laminar transport becomes important. For multiphase flows under the LHF approximation, however, the assumption is more suspect, since finite-sized dispersed-phase elements (drops or bubbles) have negligibly small laminar diffusion coefficients. Thus, the assumption can only be effective when Reynolds numbers are high, which is true for present conditions.

Neglecting effects of buoyancy in the governing equations for turbulence quantities minimizes empiricism in the turbulence model, and is adopted in the spirit of a baseline

analysis which seeks to highlight important features of the flow. Past computations using this approximation by Jeng & Faeth (1984) suggest that mean properties are not effected strongly, even when effects of buoyancy are large.

Neglecting effects of kinetic energy, viscous dissipation, and compressibility is justified for subsonic jets, but is questionable for sonic and underexpanded jets which have high Mach numbers near the passage exit. Precise analysis of the near-field region of underexpanded jets will require consideration of the shock wave field, and reduced rates of mixing of supersonic flows due to effects of compressibility (Chuech et al. 1987, 1988; Bogdanoff, 1983; Papamoschou & Roshko, 1986). However, since these processes are being highly oversimplified using the effective adapted-jet approximation, ignoring effects of kinetic energy, etc., is appropriate for such a model. Aside from potentially reduced turbulent mixing due to compressibility, the main effect of this approximation is to introduce errors in the evaluation of density. Calculations for limits of densities, having the maximum and minimum kinetic energy levels, indicated that effects of density errors were small (this will be discussed subsequently); providing some justification for the approach.

In the same manner, effects of radiation are only important where kinetic energies are high; thus, low radiation numbers in this region imply negligible effects of radiation - even for more complete analysis.

3.2 Formulation

Under the assumptions of the analysis, the conserved-scalar formalism can be used (Bilger, 1976). This involves solving governing equations for conservation of mass, mean momentum, mean mixture fraction, turbulence kinetic energy, the rate of dissipation of turbulence kinetic energy, and mixture fraction fluctuations squared. All quantities are formulated in terms of Favre averages, which are defined as follows:

$$\tilde{\phi} = \overline{\rho\phi}/\bar{\rho} \tag{3.1}$$

where an overbar indicates a conventional time average. By this definition $\phi = \tilde{\phi} + \phi''$, where $\overline{\rho\phi''} = 0$, but $\bar{\phi}'' \neq 0$ necessarily, unless the density is constant.

The Favre-averaged governing equations can be written in the following form:

$$r\partial/\partial x\,(\bar{\rho}\tilde{u}\,\phi) + \partial/\partial r\,(r\bar{\rho}v\phi) = \partial/\partial r\,((r\mu_t/\sigma_\phi)\,\partial\phi/\partial r) + rS_\phi \tag{3.2}$$

where $\phi = 1$ (for conservation of mass), $\tilde{u}$, $\tilde{f}$, k, ε and g.* The source terms, S_ϕ and the appropriate empirical constants are summarized in Table 2. The turbulent viscosity is calculated in the usual manner:

$$\mu_t = C_\mu \bar{\rho} k^2/\varepsilon \tag{3.3}$$

The flow is assumed to be fully-developed turbulent pipe flow at the passage exit, which is the initial condition for the calculations. Prescription of this state will be discussed subsequently. For this initial condition, the boundary conditions are as follows: $\tilde{u}$, $\tilde{f}$, k, ε and g are all zero at the edge of the flow; and gradients of these quantities and $\tilde{v}$ are zero at the axis.

3.3 Initial Conditions

Initial conditions require profiles of $\tilde{u}$, $\tilde{v}$, $\tilde{f}$, k, ε and g at the passage exit, along with the static pressure distribution at the exit plane. For the present simplified calculations, the effective adapted jet approximation was used; therefore, the exit plane pressure was taken to be equal to the ambient pressure. Furthermore, $\tilde{f} = 1$ and $g = 0$ at the passage exit, by definition. Measurements to be discussed later show that the test flows correspond to fully-developed pipe flows at the passage exit; therefore, $\tilde{v} = 0$ and profiles of $\tilde{u}$, k and ε can be taken from the literature for the appropriate Reynolds number (Hinze, 1975; Schlichting, 1979).

There are several effective adapted-jet approximations which have been proposed to treat the mixing properties of underexpanded jets while avoiding the complications of the external expansion region, see Chuech et al. (1987) for a review of methods proposed thus far. The divergent-nozzle approach of Kerney et al. (1972) was used during the present investigation. This involves replacing the actual external expansion process by isentropic flow to the ambient pressure, and applying the new diameter, velocities, etc., of the flow at the exit planes of the actual passage - ignoring the presence of any virtual origin. This approach has been effective for estimating the mixing properties of injection of gases into gases, and conserves mass, momentum and energy for the flow (Chuech et al., 1987). The character of the flow, fully-developed pipe flow, was preserved in the process, as recommended by Chuech et al. (1987).

---

* k, ε and g being Favre averages in this formulation.

Table 2. Summary of Source Terms in the Governing Equations

ϕ	$\mu_{eff,\phi}$	S_ϕ
1	--	0
$\tilde{u}$	$\mu + \mu_t$	$a\,(\rho_\infty - \bar{\rho})$
$\tilde{f}$	$(\mu/Sc) + (\mu_t/\sigma_f)$	0
k	$\mu + (\mu_t/\sigma_k)$	$\mu_t(\partial \tilde{u}/\partial r)^2 - \bar{\rho}\,\varepsilon$
ε	$\mu + (\mu_t/\sigma_\varepsilon)$	$[C_{\varepsilon 1}\mu_t\,(\partial \tilde{u}/\partial r)^2 - C_{\varepsilon 2}\,\bar{\rho}\,\varepsilon]\,\varepsilon/k$
g	$(\mu/Sc) + (\mu_t/\sigma_g)$	$C_{g1}\mu_t\,(\partial \tilde{f}/\partial r)^2 - C_{g2}\,\bar{\rho}\,g\varepsilon/k$

C_μ	$C_{\varepsilon 1}$	C_{g1}	$C_{\varepsilon 2} = C_{g2}$	σ_k	σ_ε	$\sigma_f = \sigma_g$	Sc
0.09	1.44	2.8	1.87	1.0	1.3	0.7	0.7

To compute effective exit conditions, the flow was taken to be an ideal gas with constant specific heats. Mach number of the equivalent exit condition is given by (Shapiro, 1954; Chuech et al. 1987):

$$M_e = [2\,(p_o/p_\infty)^{(\gamma-1)} - 1)/(\gamma - 1)]^{1/2} \tag{3.4}$$

where p_o is the stagnation pressure at the exit of the passage. Other flow properties are then found from the following expressions

$$T_o / T_e = 1 + (\gamma - 1)\, M_e^2/2 \tag{3.5}$$

$$\rho_o/\rho_e = (p_o/p_\infty)^{1/\gamma} \tag{3.6}$$

$$d_e/d = (\rho_o^2\, T_o / \rho_e^2\, M_e^2\, T_e)^{1/4} \tag{3.7}$$

$$u_e = M_e\, (\gamma\ RT_e)^{1/2} \tag{3.8}$$

3.4 State Relationships

When exchange coefficients are equal, and effects of kinetic energy and radiation are small, all instantaneous scalar properties (density, temperature, phase fractions, species concentrations, etc.) are only a function of mixture fraction. This implies that instantaneous scalar properties can be found by straightforward adiabatic mixing (or chemical equilibrium) calculations, where f kg of passage exit fluid and (1-f) kg of ambient fluid are adiabatically mixed and brought to thermodynamic equilibrium. The relationships between scalar properties and f are termed state relationships: several examples of state relationships and their construction appear in the literature (Bilger, 1976; Chen & Faeth, 1982, 1983; Faeth, 1983; Jeng & Faeth, 1984).

In the present case, state relationships constructed for isothermal mixing of air and water neglecting the small vapor pressure of water were found to be adequate; therefore, only this formulation will be shown. The mass fractions of air and water are given as

$$Y_a = f\ ,\ Y_w = 1\text{-}f \tag{3.9}$$

For isothermal mixing, the phase densities remain constant, therefore, the mixture density becomes:

$$\rho = (f/\rho_a + (1\text{-}f) / \rho_w)^{-1} \tag{3.10}$$

Finally, the void fraction is

$$\alpha = \rho f/\rho_a \tag{3.11}$$

In order to evaluate potential effects of additional property variations at high underexpansion ratios, state relationships were also constructed assuming mixing of air at the maximum effective jet exit condition considered during this investigation ($\dot{m}/\dot{m}_s = 8$). Effects of kinetic energy were also ignored for this calculation, with the static state at the passage exit taken to be equal to the ambient pressure. This results in low mixture temperatures so that the formation of ice must be considered.

State relationships for the isothermal mixing and maximum isentropic expansion states are illustrated in Fig. 10. Differences between the two state relationships are only evident at mixture fractions near unity, where ice is formed for isentropic expansion, as noted earlier. During mixing calculations, flow conditions dropped rapidly below mixture fractions where the two state relationships differ; therefore, the simple isothermal mixing approximation was adopted with little error as will be shown later.

3.5 Scalar Properties

Given state relationships, time-averaged and Favre-averaged scalar properties were found according to Bilger (1976). This involves finding a Favre-averaged probability density function of mixture fraction, $\tilde{P}(f)$, as described later. Given $\tilde{P}(f)$, the Favre-averaged mean and mean-squared fluctuating values of any scalar property become (Bilger, 1976):

$$\tilde{\phi} = \int \phi(f)\, \tilde{P}(f)\, df \tag{3.12}$$

$$\tilde{\phi}''^2 = \int (\phi(f) - \tilde{\phi})^2\, \tilde{P}(f)\, df \tag{3.13}$$

where $\phi(f)$ is the state relationship for the property ϕ. The time-averaged probability density function of mixture fraction, $\bar{P}(f)$, is related to $\tilde{P}(f)$, as follows

$$\bar{P}(f) = \bar{\rho}\, \tilde{P}(f) / \rho(f) \tag{3.14}$$

Thus, time-averaged mean and mean-squared fluctuating values of any scalar property become:

$$\bar{\phi} = \int \phi(f)\, \bar{P}(f)\, df = \bar{\rho} \int (\phi(f) / \rho(f))\, \tilde{P}(f)\, df \tag{3.15}$$

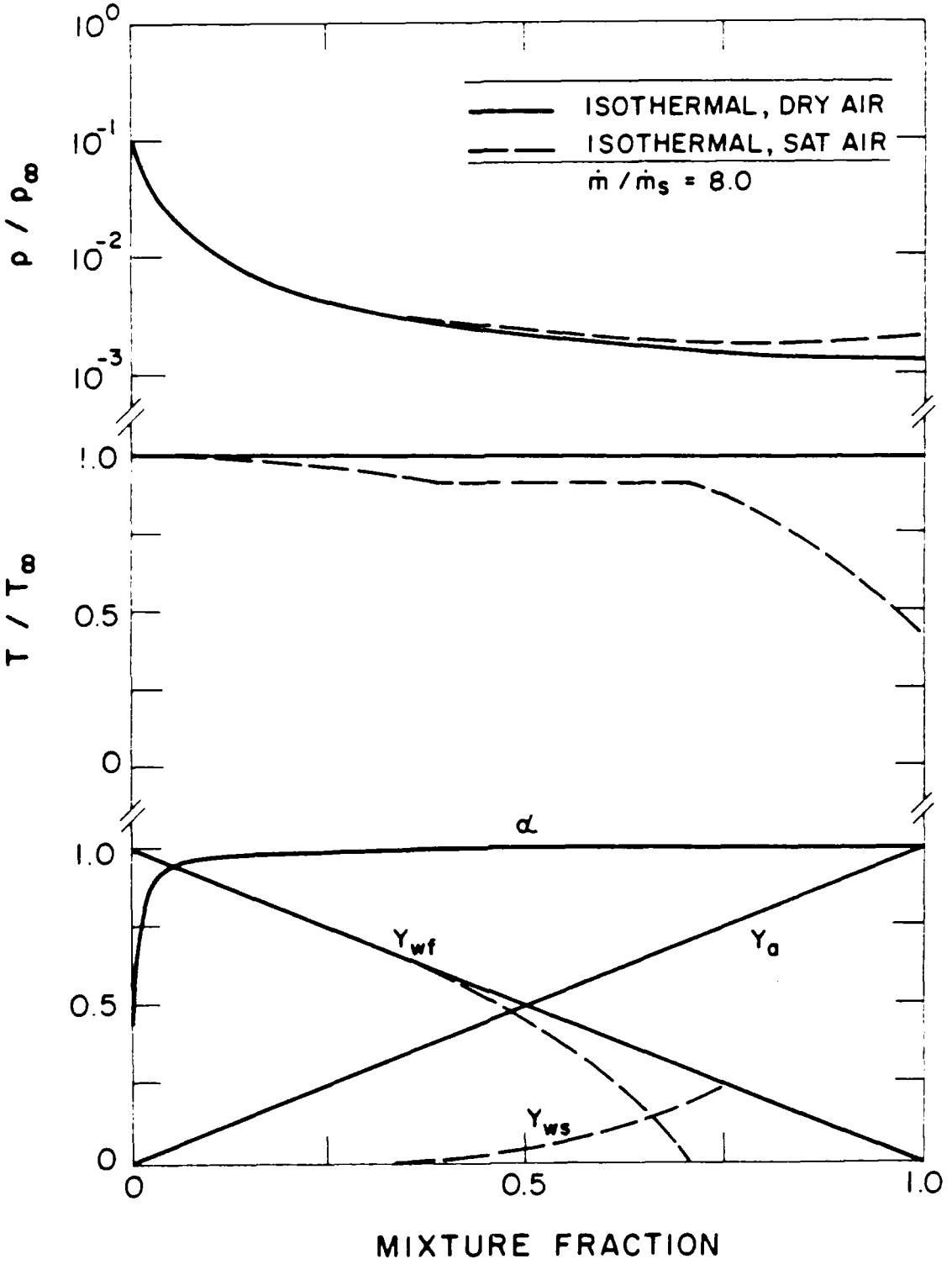

Figure 10. State relationships for air injection into water.

$$\overline{\phi}'^2 = \overline{\rho} \int ((\phi(f) - \overline{\phi})^2 / \rho(f)) \ \tilde{P}(f) + df \tag{3.16}$$

The time-averaged density, $\overline{\rho}$, which is needed to solve the governing equations, is found by setting $\phi = 1$ in equation (3.15).

To complete the formulation, a functional form must be assumed for $\tilde{P}(f)$, although the specific form does not have a strong effect on predictions (Lockwood & Naguib, 1975). Any two parameter distribution can be used, within the present level of closure, since its two unknown parameters can be found by noting

$$\tilde{f} = \int f \tilde{P}(f) \, df \tag{3.17}$$

$$g = \int (f - \tilde{f})^2 \ \tilde{P}(f) \, df \tag{3.18}$$

Since $\tilde{f}$ and g are known from the solution of the governing equations, equations (3.17) and (3.18) provide two implicit expressions to solve for the two parameters of the PDF. A clipped-Gaussian probability density function was used during the present investigation, following Lockwood & Naguib (1975) and earlier work in this laboratory (Chen & Faeth, 1982, 1983; Jeng & Faeth, 1984). Solution of the resulting transcendental equations for the most probable value and variance of this distribution was facilitated by a table constructed by Shearer et al. (1979).

3.6 Computations

Equations (3.2) were integrated using a modified version of the GENMIX algorithm due to Spalding (1977). The large density variations of the present multiphase flows required a finer numerical grid than is needed for single-phase flows. Results reported in the following used 360 cross-stream grid nodes, with streamwise step sizes chosen to be less than 0.2 percent of the current flow width, or an entrainment increase of less than 0.2 percent, whichever was limiting. Doubling the number of nodes in the mesh resulted in less than a 1 percent variation of flow properties; therefore, numerical closure was adequate, particularly in view of the other uncertainties of the analysis.

4. RESULTS AND DISCUSSION

4.1 Flow Definition

Flow Visualization. Figure 11 is a series of flash photographs of the flow for the 4.9 mm injector. A typical photograph is shown for each mass flow rate ratio that was tested. The light source was slightly to the right of the camera and tended to illuminate the right-hand side of the flow more strongly: this gives the appearance of more asymmetry of the flow in Fig. 11 than was actually observed.

At low flow rates, $\dot{m}/\dot{m}_s$ = 0.6, 1.0 and 2.0, there was significant evidence of large-scale unsteadiness of the flow. This can be seen by the bulbous regions of gas appearing in Fig. 11 for $\dot{m}/\dot{m}_s$ = 0.6 and 1.0. This behavior appeared to be associated with the release of gas at the passage exit, which also caused the gas-containing region to move below the passage exit at times. Unsteadiness decreased with increasing $\dot{m}/\dot{m}_s$, with the visible surface of the gas-containing region having finer asperities, representing the smaller turbulence length scales for higher Reynolds number flow. For $\dot{m}/\dot{m}_s$, $\geq$ 4.0, the gas-containing region rarely moved below the passage exit; instead, this behavior was replaced by a region of very rapid radial growth of the gas containing region, which is probably associated with the pressure field of the external expansion region, e.g., the growth is reminiscent of the rapid growth of the radius of the mixing layer in the first shock cell for underexpanded gas injection into gas, see Figs. 1 and 2. This rapid radial growth is particularly evident for $\dot{m}/\dot{m}_s$ = 8 in Fig. 11.

Consecutive photographs from a high-speed motion picture film (roughly 1 picture/ms) of the flow for $\dot{m}/\dot{m}_s$ = 8 appear in Fig. 12. This type of behavior was typical of operation most of the time for high underexpansion ratios. The flow near the passage exit exhibits a deformed liquid surface, with asperities probably caused by the underlying turbulent flow. However, operation near the passage exit is relatively steady with little evidence of pulsing of the liquid into the passage or the presence of gas below the passage exit.

Even for relatively high underexpansion ratios, however, there were occasions when the flow was strongly disturbed near the external expansion region. An occurrence of this type can be seen in the consecutive photographs from a high-speed motion picture film (roughly 1 picture/ms) of the flow for $\dot{m}/\dot{m}_s$, = 2, appearing in Fig. 13. The disturbance appears within 1 ms, and disappears again in 3 ms, for the conditions of the photographs. It takes the form of a sharp cut, or necking down, of the flow, which pushes gas down over the outside of the flow passage. These occurrences were random and appear to be the same type of disturbance as the "reverse shocks" mentioned by Surin, et al. (1983). They hypothesize that the behavior is due to instability of the air-liquid

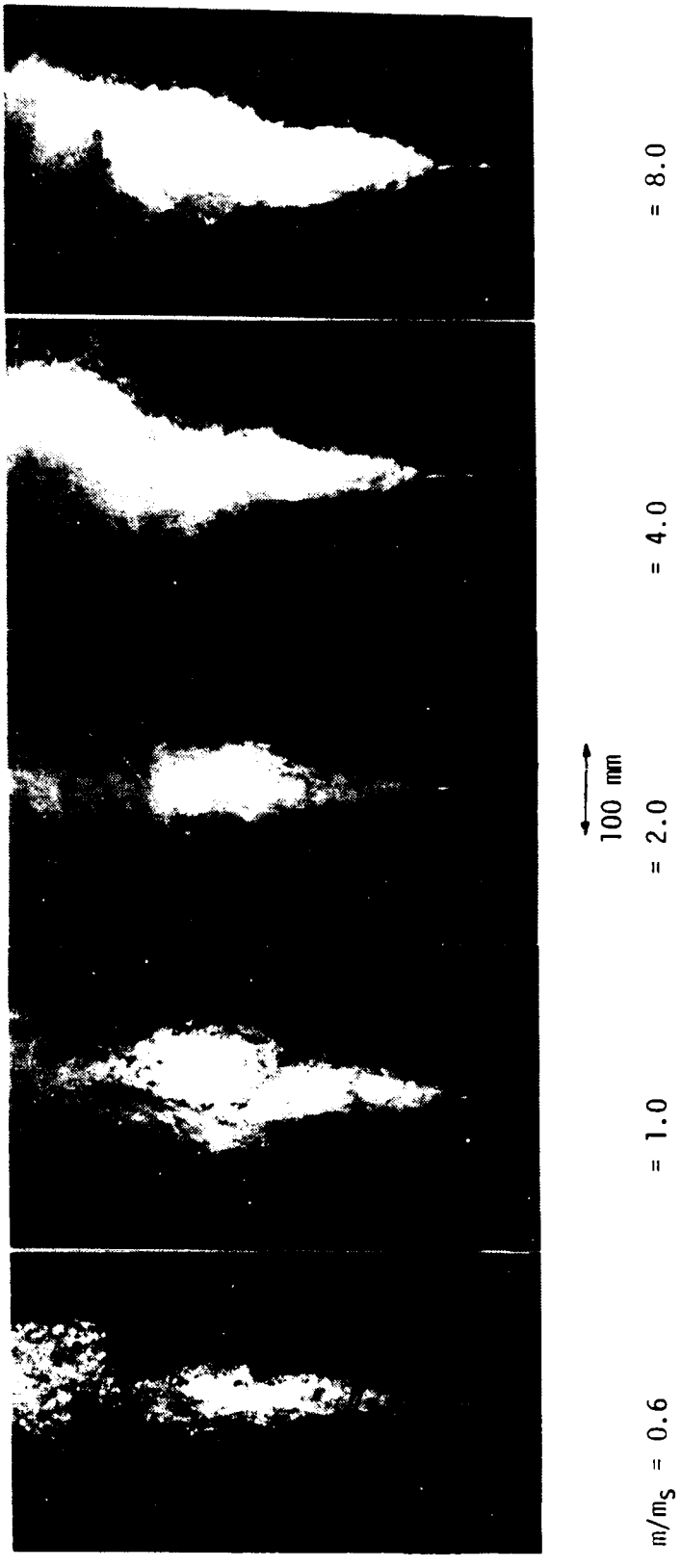

Figure 11. Flash photographs of flow for various mass flow ratios (4.9 mm passage diameter).

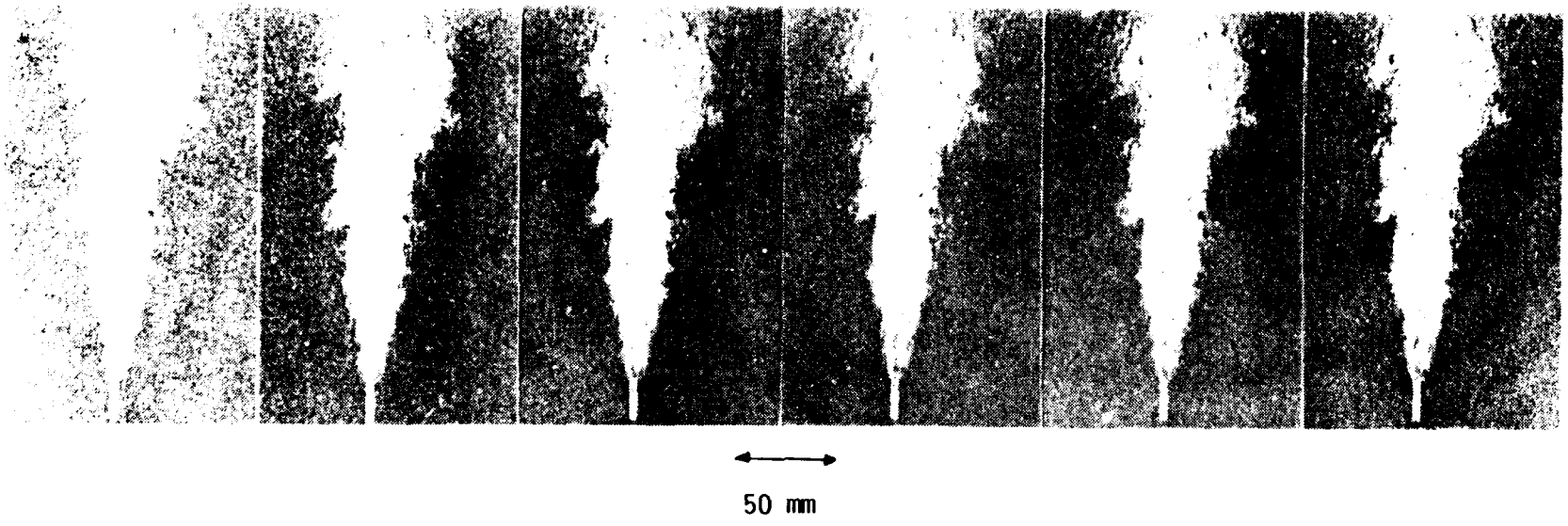

Figure 12. Motion-picture sequence for stable injection 4.9 mm passage diameter, mass flow ratio of 8).

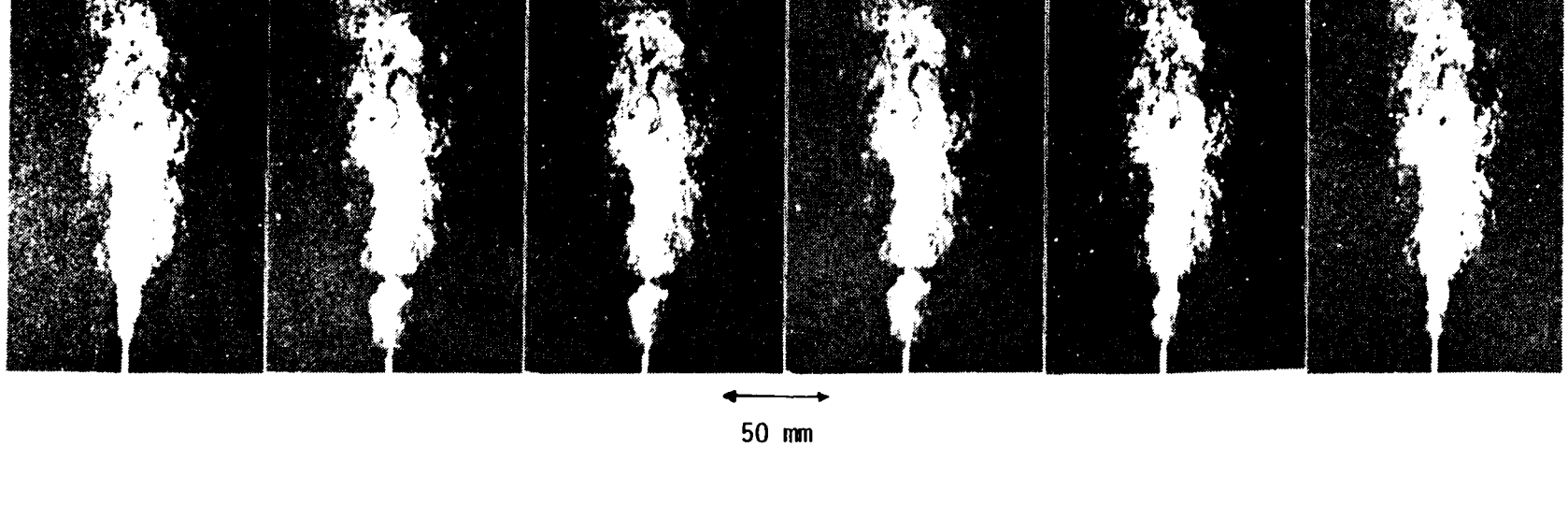

Figure 13. Motion-picture sequence showing a reverse shock (4.9 mm passage diameter, mass flow ratio of 2).

interface, producing a hydraulic jump as large eddies constrict the flow at the passage exit. Certainly the rapidity of the event, in comparison to other turbulent mixing processes that can be seen in Figs. 12 and 13, suggests a process associated with a shock wave structure.

The motion pictures were analyzed to find the disturbance frequencies near the passage exit. These frequencies are plotted as a function of $\dot{m}/\dot{m}_s$, in Fig. 14, for the 4.9 mm diameter passage. At values of $\dot{m}/\dot{m}_s$ = 0.6 and 1.0, the pulsing of the flow was relatively periodic, but became more random and less frequent at $\dot{m}/\dot{m}_s$ = 4.0 and 8.0. The pulsation frequency reached a maximum of roughly 20 Hz for $\dot{m}/\dot{m}_s$ = 1.0, declining to roughly 3 Hz at $\dot{m}/\dot{m}_s$, = 8.0. This behavior, and the motion picture photographs of the flow, suggest that two phenomena are responsible for the unsteadiness: slugging into the passage at low flow rates, with frequencies related to jet velocities; and reverse shock, disturbances (remote from the passage exit) associated with the external expansion region of highly underexpanded jets.

Plenum Pressure Fluctuations. The idea that two unsteady mechanisms are present is supported by the plot of plenum pressure fluctuations, as a function of $\dot{m}/\dot{m}_s$, in Fig. 14. Relative plenum pressure fluctuations are largest at low flow rates, suggesting slugging of liquid into the injector passage at these conditions. At high flow rates, however, plenum pressure fluctuations become relatively low. This indicates that the external expansion region tends to isolate the flow passage from flow disturbances in the bath. However, portions of the external expansion region are still subject to reverse-shock unsteadiness. Determining the origin and behavior of these unsteady phenomena represents a challenging problem, requiring more information than is currently available (or will be provided by the present report) to gain an understanding of it. Fortunately, reverse shocks are an infrequent fast event for large values of $\dot{m}/\dot{m}_s$; therefore, continuing to interpret the flow as being stationary is reasonable.

Passage Exit Conditions. Flow properties at the passage exit were measured for air injection in still air; therefore, unsteadiness associated with injection into a liquid was not a factor. Time-averaged streamwise mean and fluctuating velocities at the passage exit, for both passages and all expansion ratios tested, are illustrated in Figs. 15 and 16. The same properties for fully-developed pipe flow, measured by Nikuradse and Laufer, and cited in Hinze (1975) and Schlichting (1979), are also plotted on the figures.

Present measurements near the axis agree quite closely with the findings of Nikuradse and Laufer, supporting the idea that present jet exit conditions approximated fully-developed pipe flow -- at least when the flow is steady. For $\dot{m}/\dot{m}_s$ = 0.6 and 1.0, however, this agreement extends to near the edge of the flow, but the measurements subsequently become somewhat broadened. This occurs since the measuring plane was at x/d = 0.2, to avoid cutting the laser beams of the LDA with the passage exit, allowing some

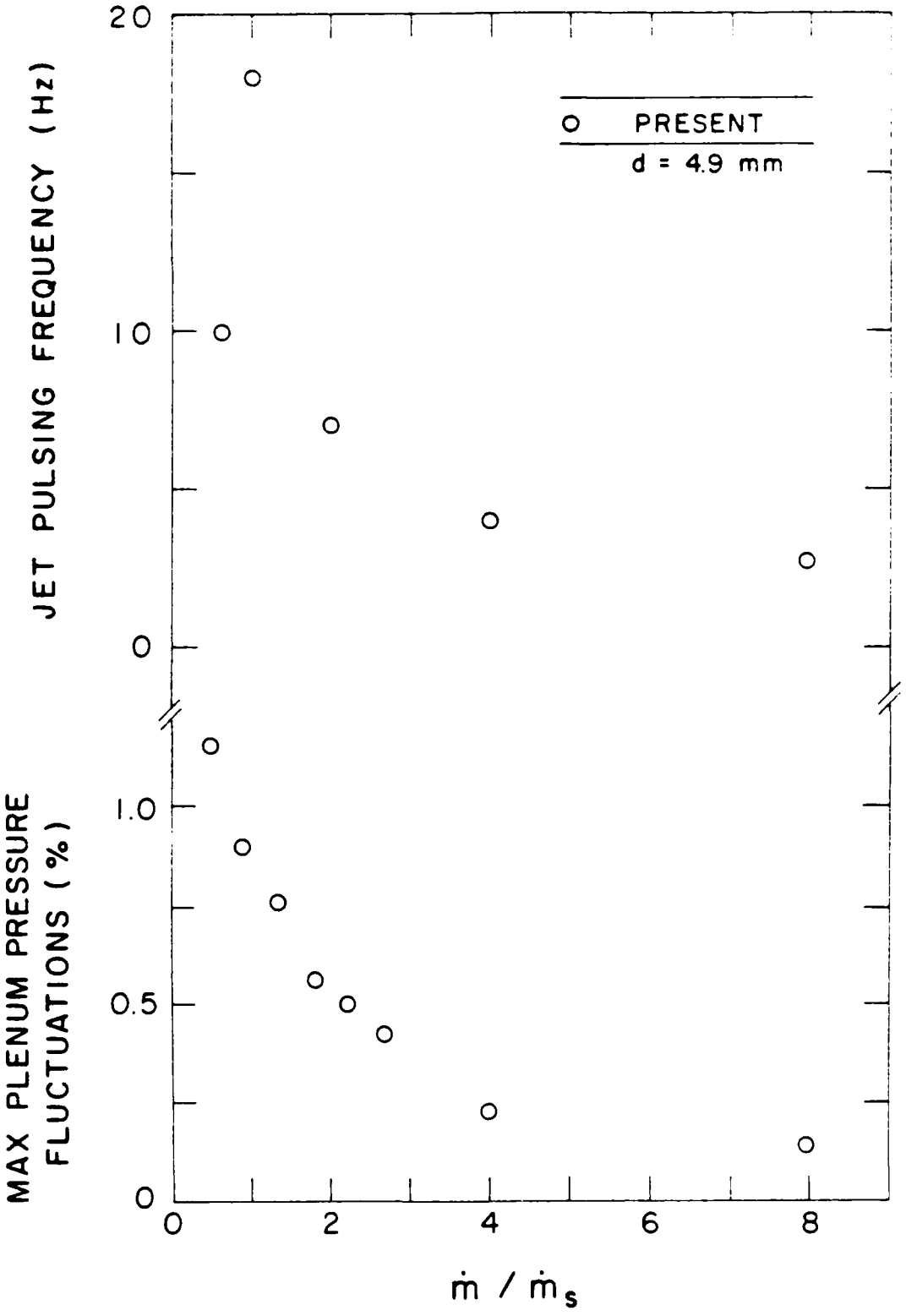

Figure 14. Injector pulsing frequency and maximum plenum static pressure fluctuations vs. mass flow ratio (4.9 mm passage diameter).

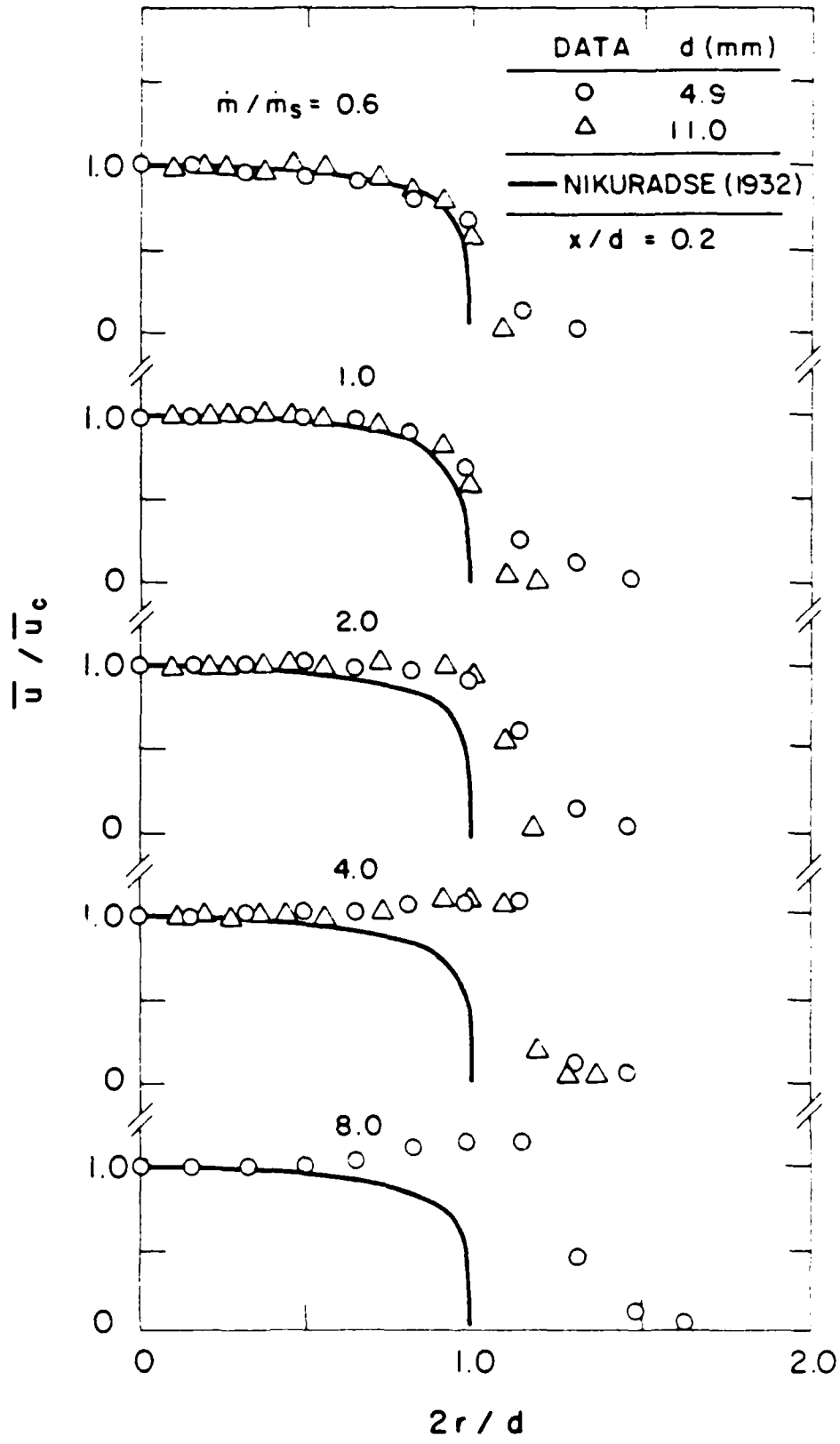

Figure 15. Streamwise mean velocities near jet exit (air injection into air.)

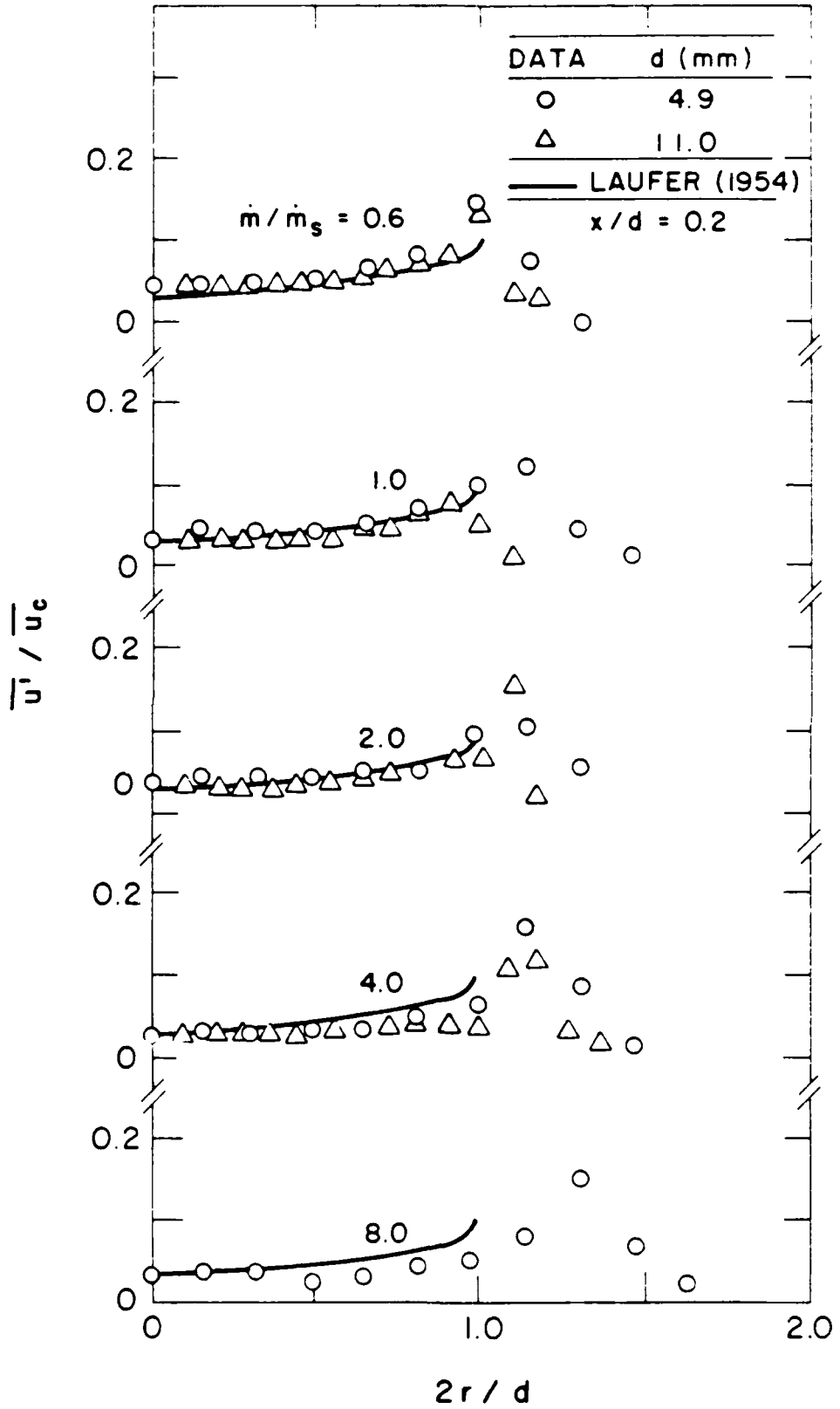

Figure 16. Streamwise velocity fluctuations near jet exit (air injection into air).

build up of the mixing layer near the edge of the flow before the measuring plane was reached.

The character of the velocity profiles in Figs. 15 and 16, particularly the mean velocity profiles, changes dramatically as $\dot{m}/\dot{m}_s$, increase above unity. This behavior is due to the acceleration of the flow as it passes through the expansion fan which eminates from the passage wall at its outlet, see Figs. 1 and 2. Similar behavior has been observed by Chuech et al. (1987, 1988) for underexpanded air jets in air. Based on the portion of the velocity profiles near the axis, the passages still appear to provide very nearly fully-developed pipe flow at the exit, which is reasonable in view of their length.

4.2 Flow Structure

Static Pressures. Static pressures along the axis, for $\dot{m}/\dot{m}_s = \geq 1.0$, are illustrated in Fig. 17. Results are shown for injection into both air and water, from the same 11.0 mm diameter passage. The results for injection into air are very similar to the findings of Chuech et al. (1987, 1988) for underexpanded fully-developed pipe flows in still air. Static pressures along the axis exhibit a decaying oscillatory behavior due to the presence of shock cells that eventually decay away as the mixing layers near the edge of the flow reach the axis. The amplitude of these pressure oscillations progressively increase as $\dot{m}/\dot{m}_s$ increases. For $\dot{m}/\dot{m}_s$ 1.2 and 1.4, Chuech et al. (1987, 1988) find that these pressure oscillations are observable up to $x/d < 7 - 10$. Present measurements do not extend this far in the streamwise direction, but pressure amplitudes and the wavelengths of the pressure oscillations agree quite closely with those of Chuech et al. (1987, 1988) for $\dot{m}/\dot{m}_s$,= 1.2 and 1.4.

The most interesting feature of the results illustrated in Fig. 17 is that static pressure variations along the axis for injection of air into water are very similar to those observed for injection of air into air, at least for the first one or two shock cells. With increasing $\dot{m}/\dot{m}_s$, the similarity of the two static pressure records progressively extends farther into the flow field, reaching $x/d = 2\text{-}3$ for $\dot{m}/\dot{m}_s = 4.0$. This is clear proof that a shock wave containing external expansion region is present for underexpanded air jets in water

The main differencc between the static pressure records for underexpanded injection of air into air and into water, is that the external expansion region decays more rapidly for injection of air into water. This behavior is expected, since turbulent mixing is invariably more rapid for injection of air into water than for air into air (Chen & Faeth, 1982, 1983). The greater length of the external expansion region for higher values of $\dot{m}/\dot{m}_s$ is probably due to the larger density ratio of the flow. Reduced rates of mixing in supersonic turbulent flows (Bogdanoff, 1983; Papamoschou & Roshko, 1986) may also be a factor.

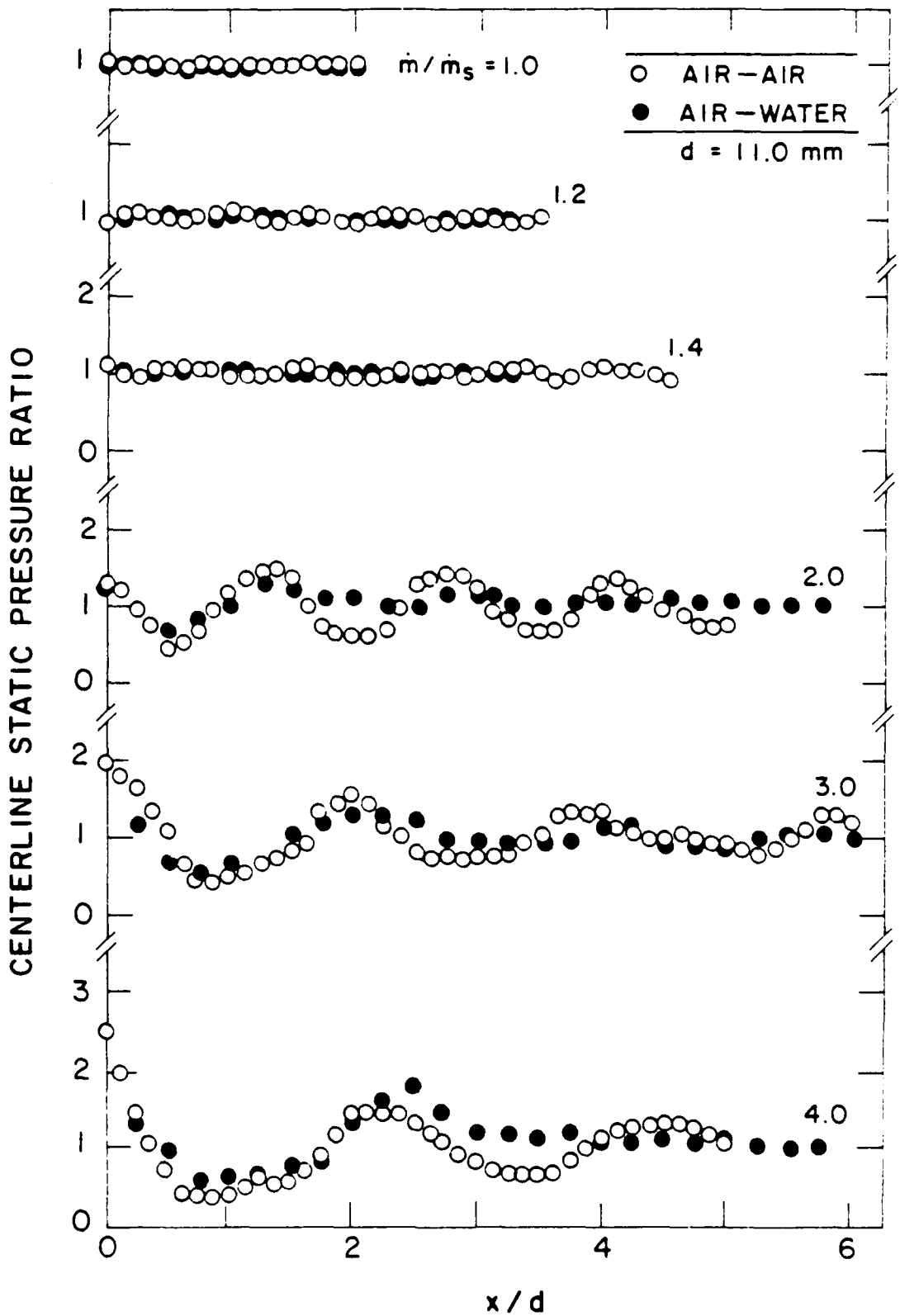

Figure 17. Static pressures along axis for various mass flow ratios (11.0 mm passage diameter).

Another comparison between aspects of the shock wave field of underexpanded air jets in air and in water is illustrated in Fig. 18. Here, the length of the second shock cell is plotted as a function of $\dot{m}/\dot{m}_s$. Along with present measurements for injection into air and into water, results from Chuech et al. (1987, 1988) and Seiner & Norum (1980) for injection of air into air are also shown. The results of all studies for air injection into air are similar, with the length of the second shock cell progressively increasing with increasing $\dot{m}/\dot{m}_s$. The length of the second shock cell for air injection into water follows the same trend, however, the length is generally larger in this case. Such behavior suggests increased effective Mach numbers in the flow, which could result from the lower acoustic velocities observed in multiphase flows -- at least at the LHF limit.

Void Fractions. Time-averaged void fractions along the axis for air injection into water are illustrated in Fig. 19 for the 4.9 mm diameter passage. In addition to the present measurements, the probe measurements of Tross (1974) are also shown for $\dot{m}/\dot{m}_s = 1.0$ and 2.0. Finally, predictions using the LHF approximation also appear on the plot. It was found that use of either state relationship, appearing in Fig. 10, and either fully-developed or slug flow at the passage exit, yielded essentially the same results. This behavior is quite different than experience for liquid injection into gases under the LHF approximation (Ruff et al., 1988; Lee et al., 1979) where the initial state of flow development at the passage exit has a substantial influence on subsequent turbulent mixing properties. This behavior follows from the higher inertia of the liquid for liquid injection, due to its greater density, which provides a means of carrying significant levels of turbulence energy into the flow field, enhancing mixing, compared to gas injection.

Examining the measurements in Fig. 19, it is clear that higher underexpansion ratios (higher $\dot{m}/\dot{m}_s$) result in progressively reduced mixing rates along the axis. This deferral of mixing is apparently the price that must be paid in order to obtain more stable injector operation with increasing $\dot{m}/\dot{m}_s$. In the region where they can be compared, the measurements of Tross (1974) are consistently lower than present measurements -- particularly far from the injector. Such behavior is expected, since all biases encountered with probes tend to reduce observed void fractions (Tross, 1974). It is felt that the present nonintrusive gamma-ray absorption measurements are more reliable.

The comparison between present measurements and predictions is encouraging for $\dot{m}/\dot{m}_s \geq 2$, where effects of unsteadiness of the flow are relatively small. It is unfortunate, however, that the observed agreement between predictions and measurements for $\dot{m}/\dot{m}_s \geq 2$ involves effects of both the locally-homogeneous flow approximation and the effective adaptive jet approximation; therefore, a fortuitous cancellation of errors introduced by both approximations cannot be discounted. For $\dot{m}/\dot{m}_s \leq 1$, however, measure void fractions are consistently below predictions for $x/d > 10 - 20$, suggesting underestimation of turbulent

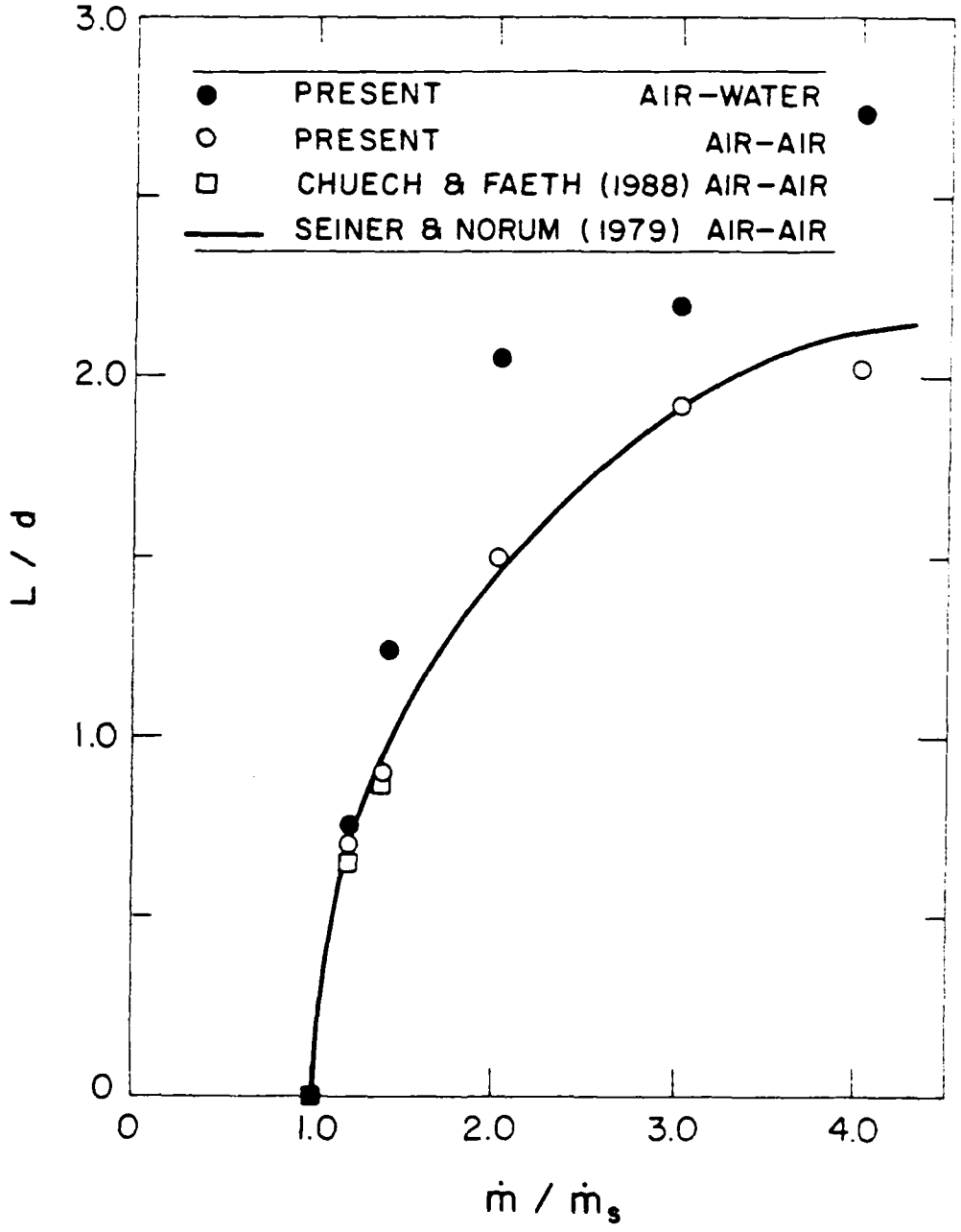

Figure 18. Secondary shock-cell spacing vs. mass flow ratio (11.0 mm passage diameter).

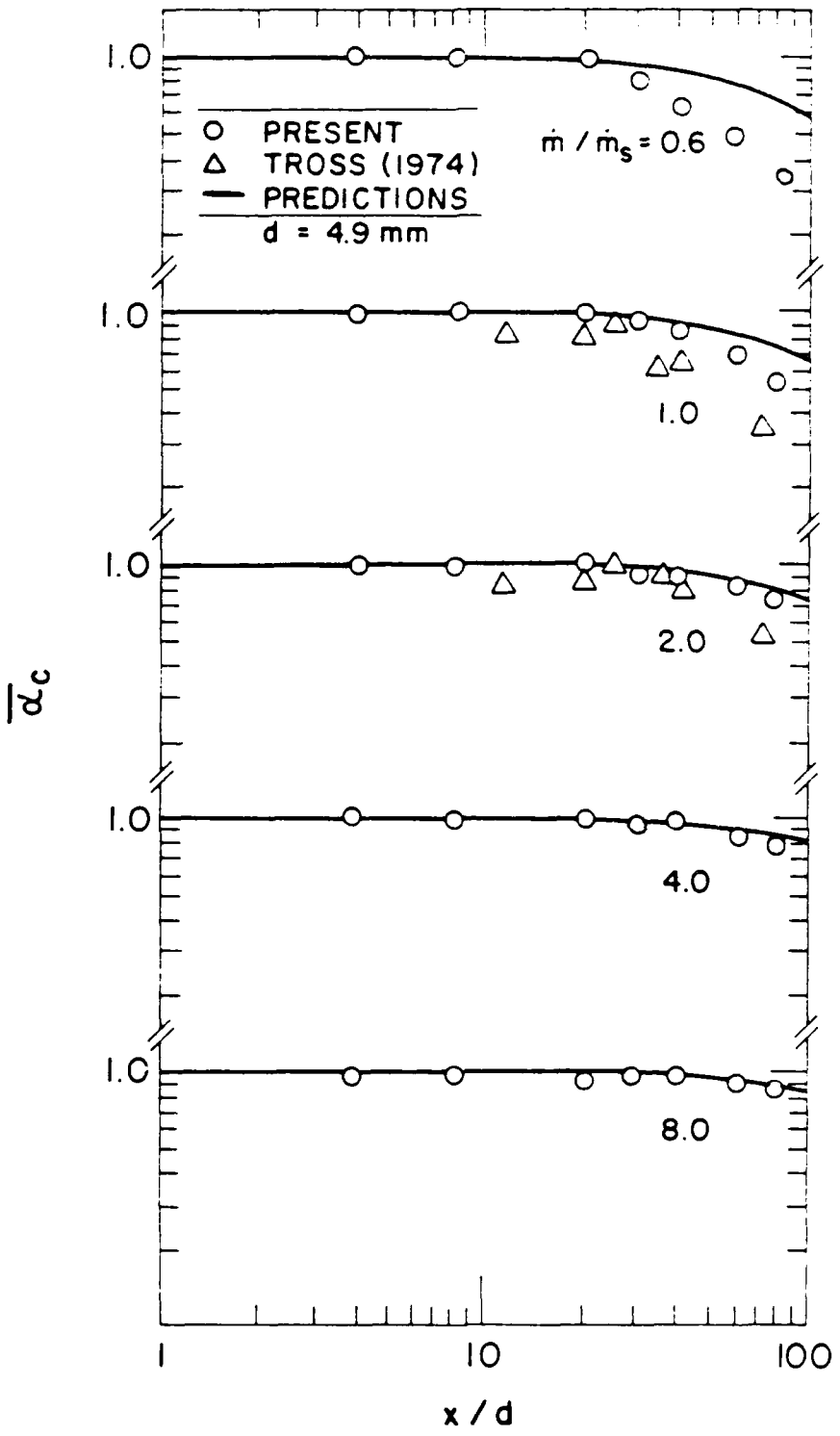

Figure 19. Time-averaged void fractions along axis for various mass flow ratios.

mixing by the predictions. This cannot be due to the LHF approximation, which invariably causes the mixing rates of multiphase flows to be overestimated (Faeth, 1983). Instead, effects of flow unsteadiness at low flow rates, which would be expected to enhance mixing rates due to transient phenomena, are more likely to be responsible for the observed behavior.

Measured and predicted radial distributions of time-averaged void fractions are illustrated in Figs. 20-24, for all values of $\dot{m}/\dot{m}_s$ tested. The results are plotted as a function of r/x, which is the radial similarity variable for fully-developed single-phase turbulent jets, so that the actual width of the flow can be seen. In addition to the present data for 4.9 and 11.0 mm diameter passages, results from Tross (1974) are also shown for $\dot{m}/\dot{m}_s$ = 1.0 and 2.0. The most striking feature of the measurements illustrated in Figs. 21-25 is the unusual width of the void fraction profiles. This is expected near the passage exit when results are plotted as a function of r/x, however, this behavior persists even at x/d = 80, where the flow might be expected to approach the properties of fully-developed jets. Yet even at x/d = 80, void fraction flow widths approach r/x ~ 0.3, which is nearly twice the width observed for properties in single-phase jets (Wynanski & Fiedler, 1969). One reason for this behavior is that void fraction is an unusually sensitive indicator of the mixing level of the flow, at low void fractions. For example, when $f << \rho_a/\rho_w$, equation (3.11) becomes

$$\alpha \simeq \rho_w f / \rho_a \tag{4.1}$$

For present test conditions, $\rho_w / \rho_a \sim 1000$; therefore, α is an extremely sensitive function of mixture fraction and as a result α is still significant even when f is much smaller than values of mixing levels that would normally be associated with the edge of a jet.

The measured radial profiles of α illustrated in Figs. 20-24 change surprisingly little near the passage exit as $\dot{m}/\dot{m}_s$ varies. It appears that unsteadiness at low $\dot{m}/\dot{m}_s$ contributes to flow widths near the injector exit in roughly the same manner as underexpansion at high value of $\dot{m}/\dot{m}_s$ The probe measurements of Tross (1974), for $\dot{m}/\dot{m}_s$ = 1.0 and 2.0 are roughly the same as the present measurements, although the probe measurements are quite scattered. This provides some support for the present findings, although the support is weak due to the large uncertainties associated with the use of probes in multiphase jets.

The comparison between predictions and measurements in Figs. 20-24 is encouraging, in the sense that predicted characteristic flow widths tend to scale with the measurements as x/d and $\dot{m}/\dot{m}_s$ vary. However, the shapes of the predicted profiles are far too blunt in the radial direction, particularly near the passage exit. There was concern that the strong sensitivity of α to f, shown by equation (4.1), might be responsible for this behavior, due to truncation errors in the calculations. However, careful review of this

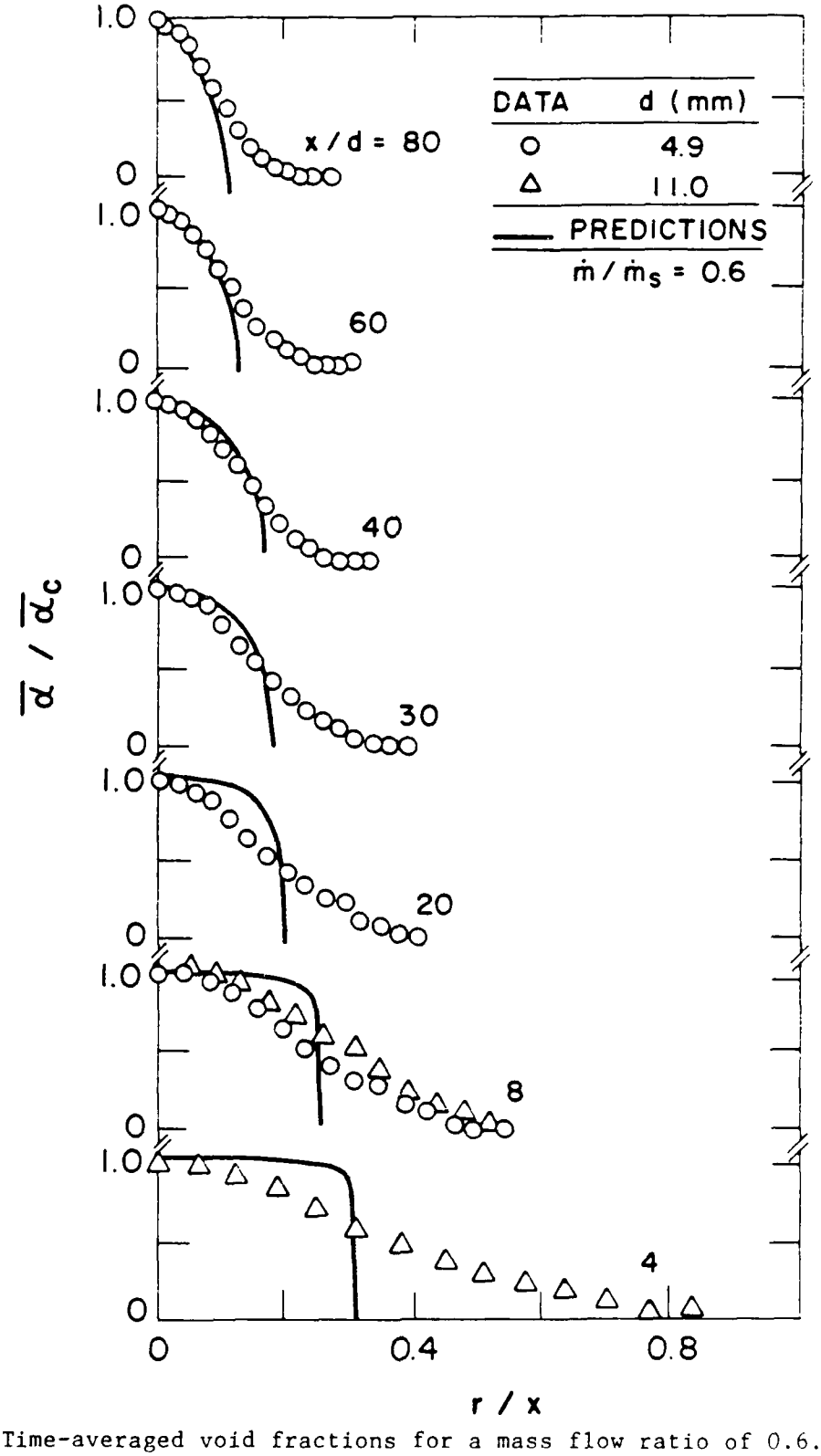

Figure 20. Time-averaged void fractions for a mass flow ratio of 0.6.

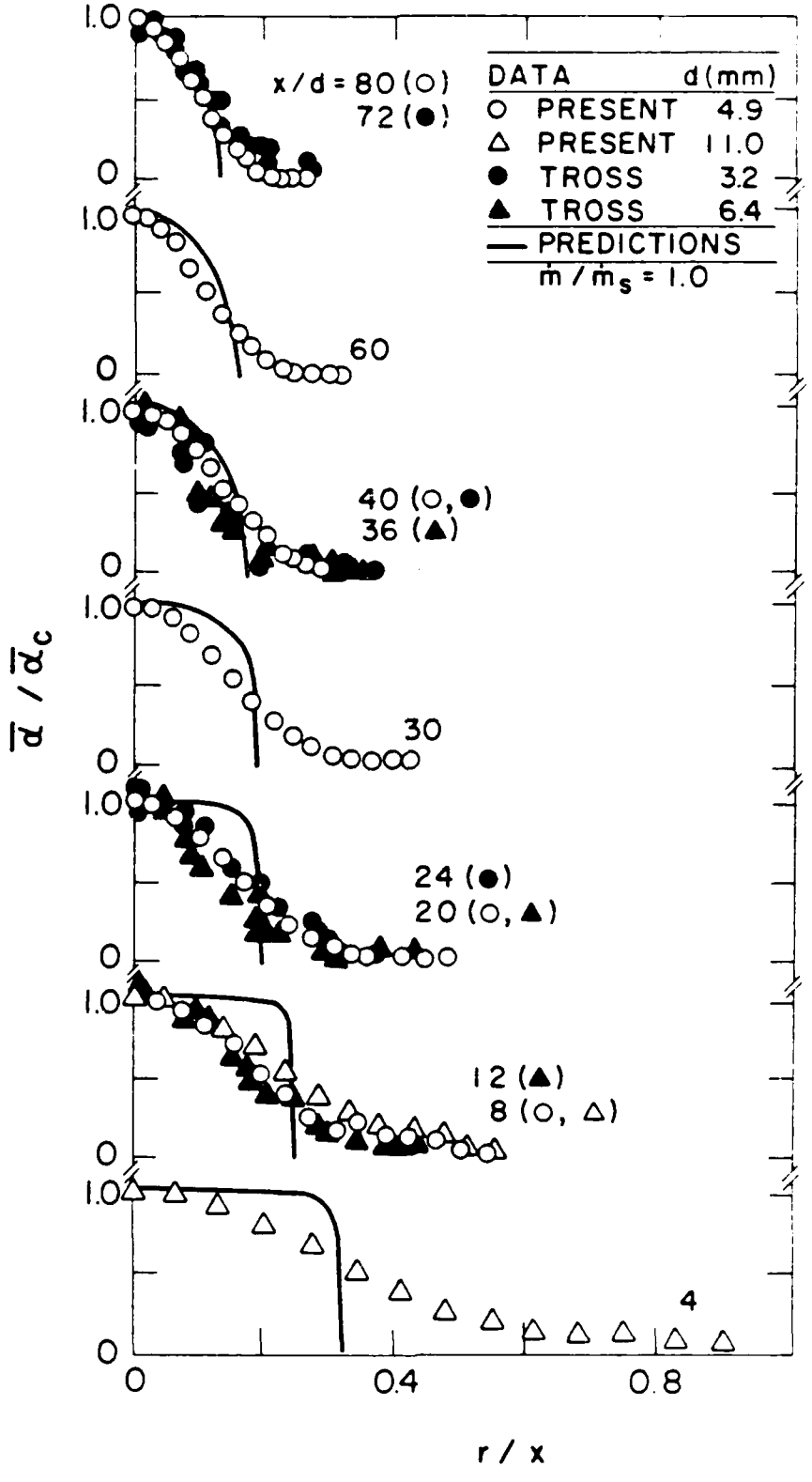

Figure 21. Time-averaged void fractions for a mass flow rate ratio of 1.0.

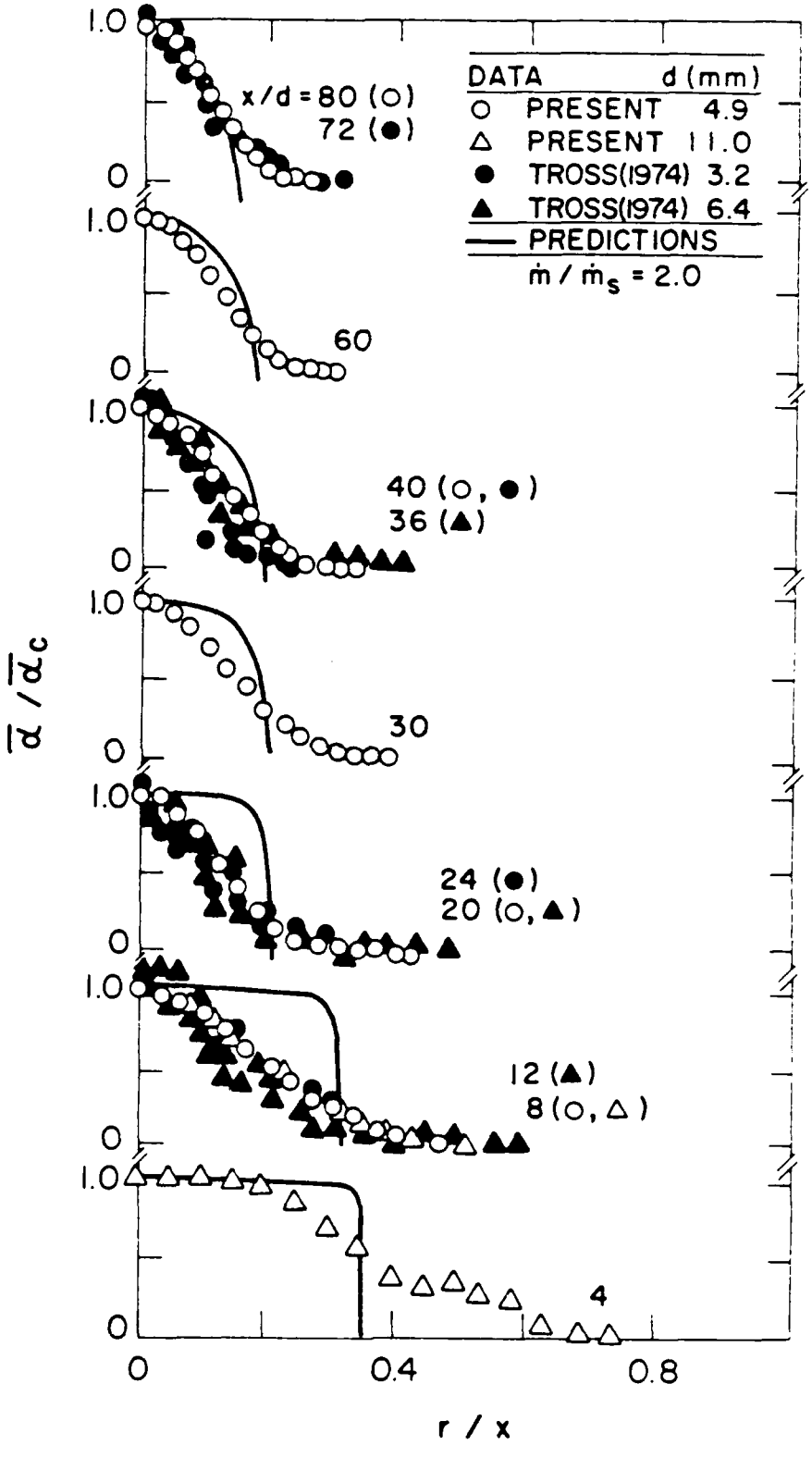

Figure 22. Time-averaged void fractions for a mass flow rate ratio of 2.0.

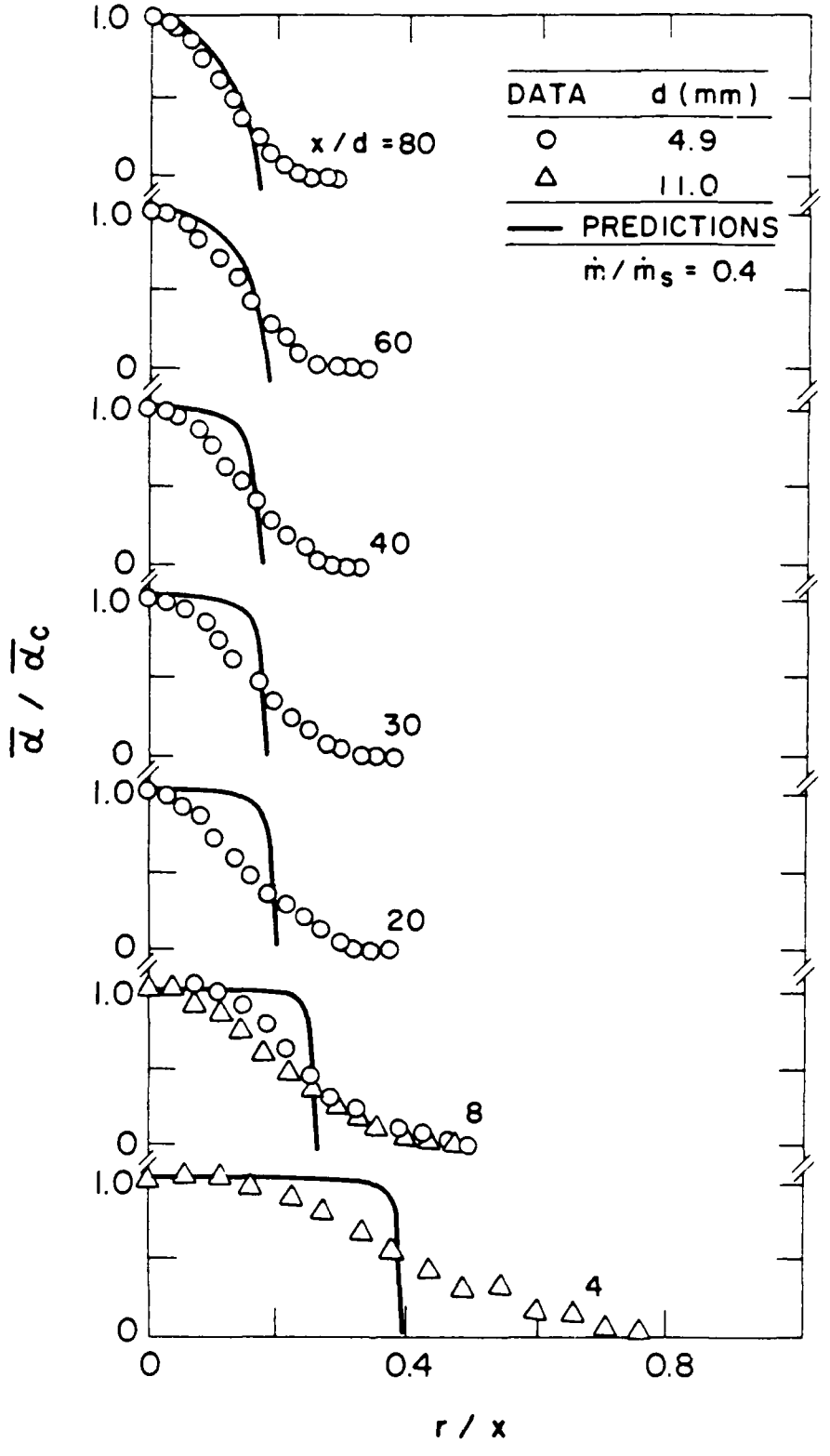

Figure 23. Time-averaged void fractions for a mass flow rate ratio of 4.0.

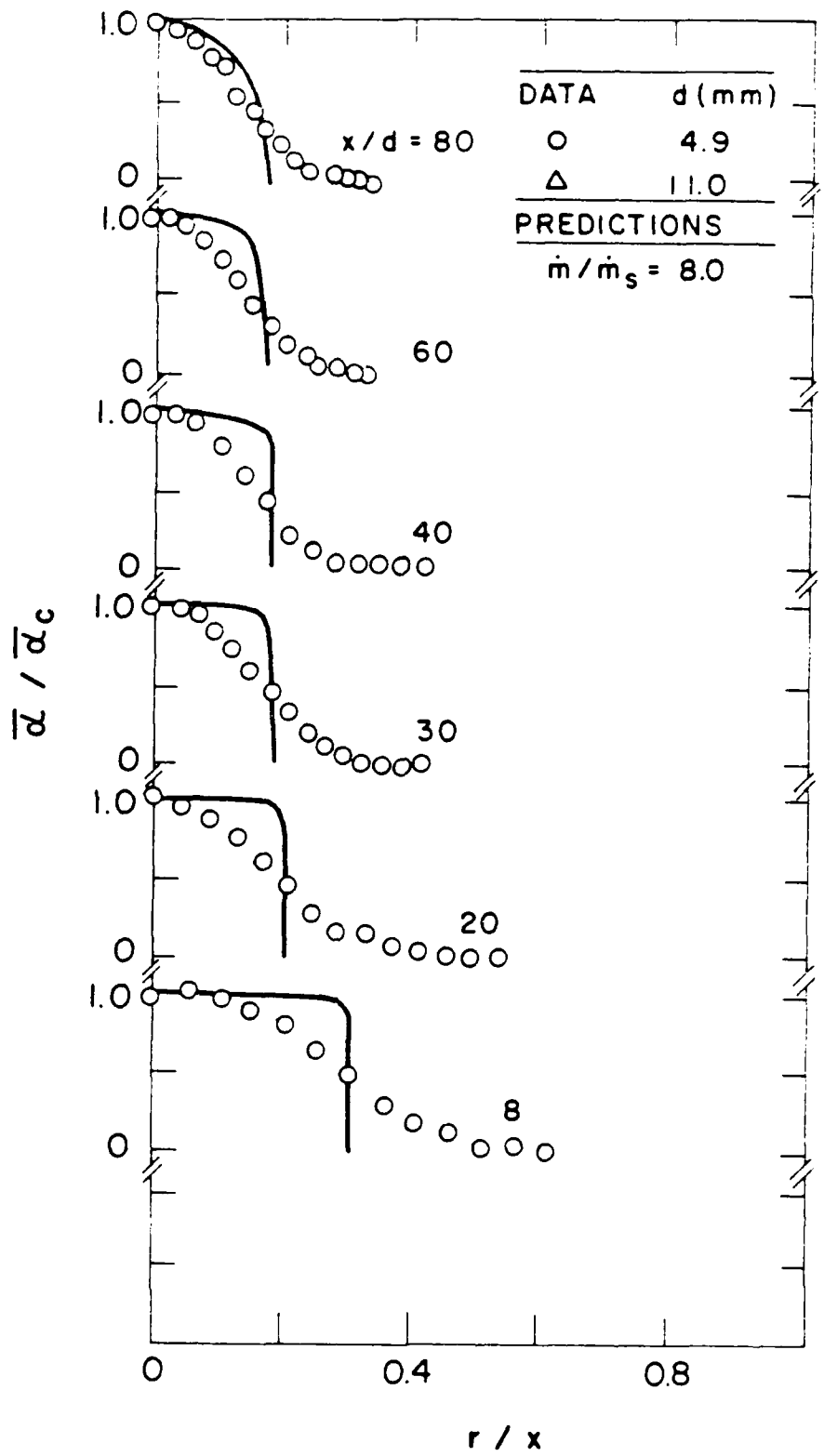

Figure 24. Time-averaged void fractions for a mass flow rate ratio of 8.0.

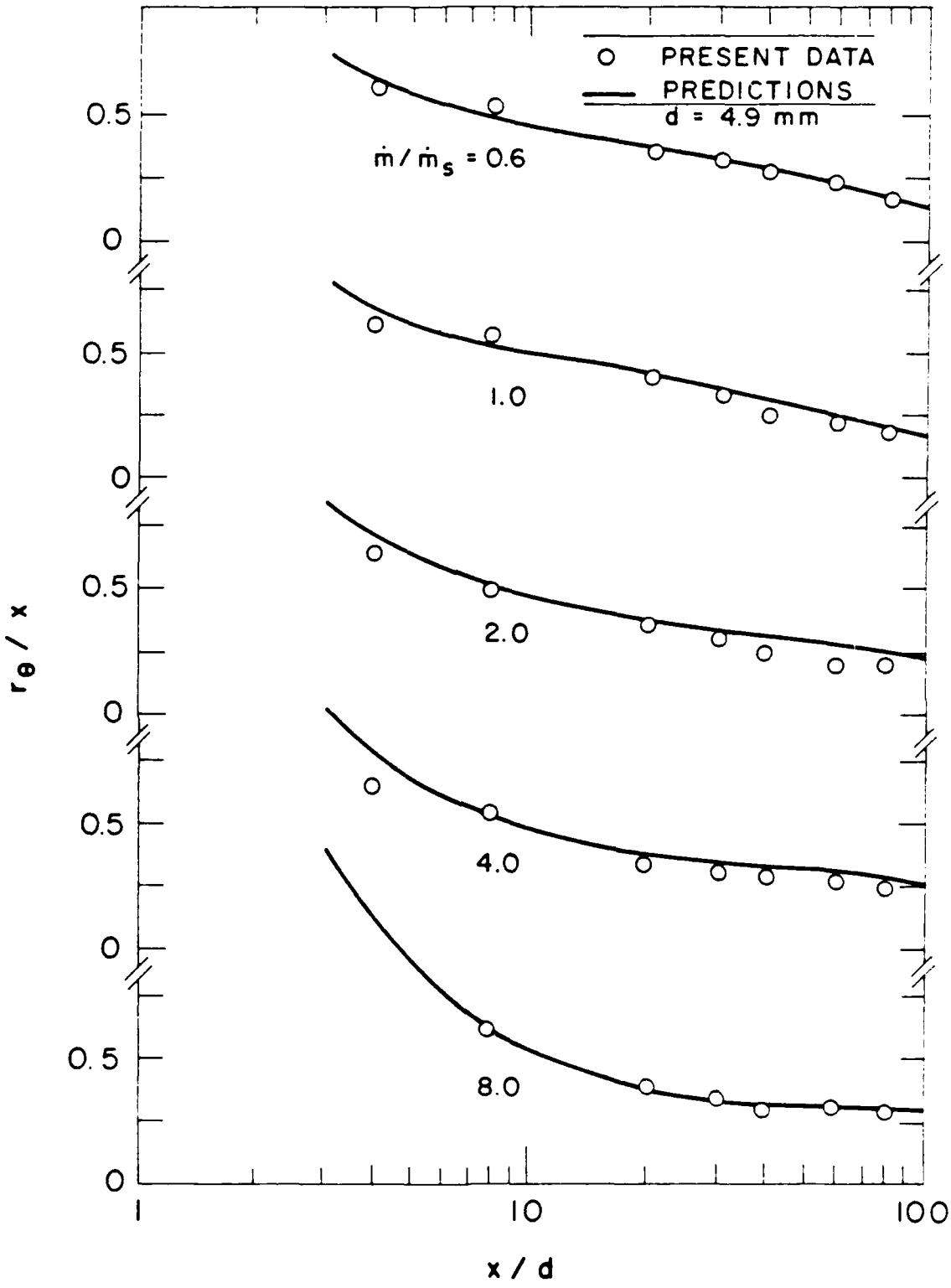

Figure 25. Streamwise variation of jet width for various mass flow ratios (4.9 mm passage diameter).

aspect of the calculations did not reveal any deficiencies. Thus, while the discrepancy is may be related to the unusual sensitivity of α to f, it also suggests a defect of the basic analysis or a possible effect of unsteadiness and reverse shocks on the mixing properties of the flow.

Figure 25 is an illustration of characteristic flow width r_e (where the half width is defined as the point where $\alpha/\alpha_c = 0.5$), plotted as a function of x/d for various $\dot{m}/\dot{m}_s$ for the 4.9 mm diameter passage. The unusual width of the flow, when viewed in terms of α, is evident from the figure. The characteristic flow width also increases everywhere as the degree of underexpansion increases, e.g. at x/d = 80, $r_e/x \sim 0.2$ for $\dot{m}/\dot{m}_s = 0.6$ increasing to $r_e/x \sim 0.3$ for $\dot{m}/\dot{m}_s = 8.0$. Although the shape of the radial profiles of time-averaged void fraction is not predicted very well, the comparison between predicted and measured characteristic flow widths is excellent.

Measured entrainment coefficients, defined according to equation (2.2), are plotted in Fig. 26. Present predictions, as well as the entrainment coefficient correlation of Ricou & Spalding (1961), are also plotted on the figure for comparison with the measurements. The correlation of Ricou & Spalding (1961) was measured in the fully-developed region of single-phase variable-density round jets, for circumstances where effects of buoyancy are small: in this case similarity implies that the entrainment coefficient is constant. Measured entrainment coefficients generally increase with increasing x/d, and decrease at all axial stations with increasing $\dot{m}/\dot{m}_s$. The increase with increasing x/d is due to effects of buoyancy, which influence flow properties nearer to the passage exit at lower values of $\dot{m}/\dot{m}_s$, where the initial streamwise momentum of the flow is smaller. The reduction of the entrainment coefficient with increasing $\dot{m}/\dot{m}_s$, near the passage exit where buoyancy is not a factor, could be related to the reduction of turbulent mixing for supersonic compressible shear layers (Bogdanoff, 1983; Papamouschou & Roshko, 1986).

The comparison between present predictions and measurements of entrainment coefficients in Fig. 26 is generally not very good, although predictions tend to improve somewhat as $\dot{m}/\dot{m}_s$ and x/d increase. For low values of $\dot{m}/\dot{m}_s$, the large increase of the measured entrainment coefficients over predictions is probably due to effects of unsteadiness of the flow, which would be expected to increase mixing rates. Accordingly, this discrepancy seems to persist at a lesser degree at high $\dot{m}/\dot{m}_s$, particularly near the passage exit. Unsteadiness, rather than difficulties with the LHF approximation appears to be the most logical explanation of the results illustrated in Fig. 26, since the LHF approximation invariably causes mixing rates to be overestimated.

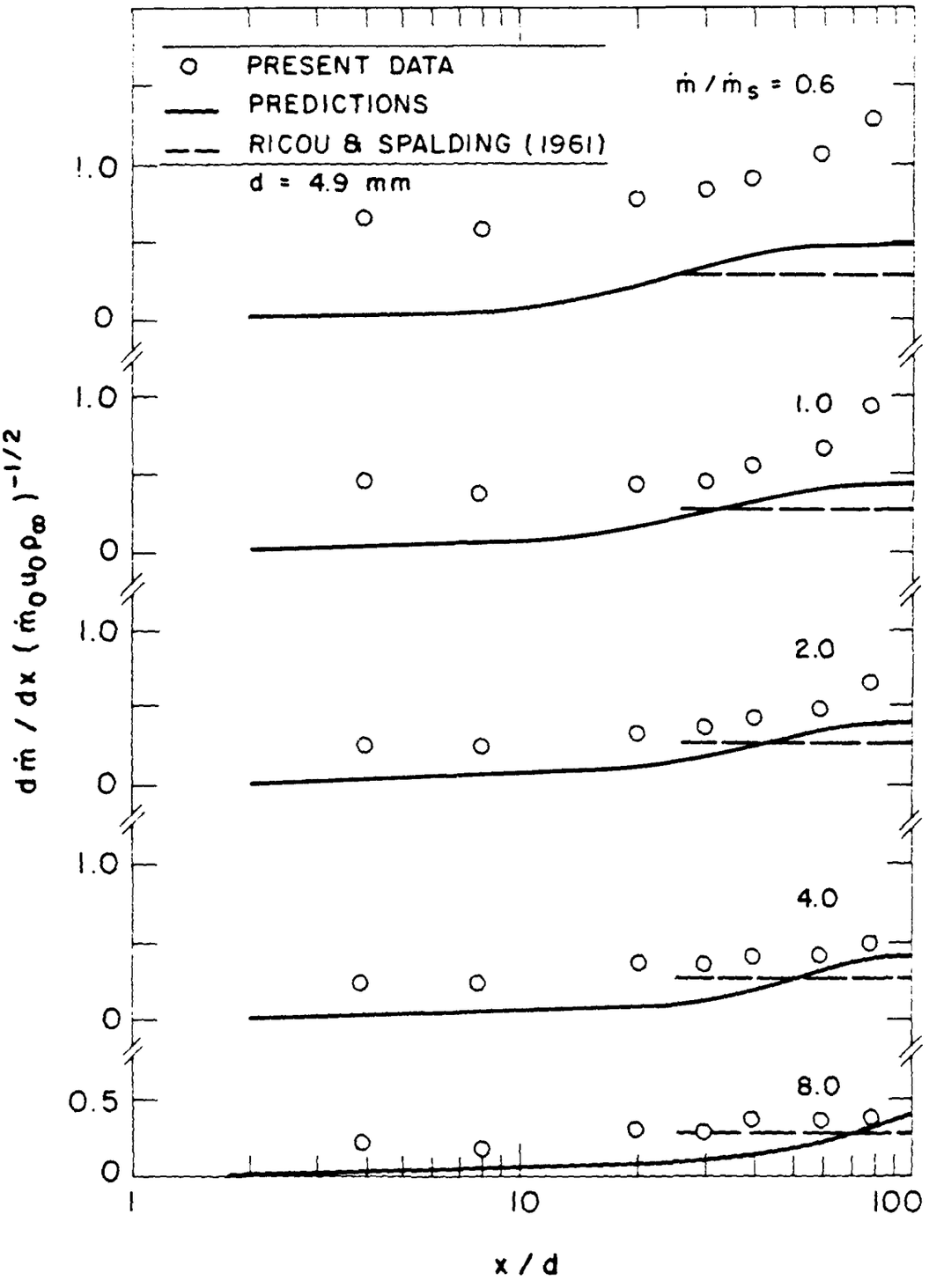

Figure 26. Streamwise variation of entrainment coefficient for various mass flow ratios (4.9 mm passage diameter).

5. CONCLUSIONS

Major conclusions of the present study are as follows:

1. Shock wave containing external expansion regions are present for underexpanded air jets in water, similar to air jets in air, however, the more rapid mixing rate for air jets in water causes the external expansion region to decay more rapidly. The strong pressure fields associated with this region probably play a role in stabilizing the unsteadiness of these flows at large $\dot{m}/\dot{m}_s$.

2. Increasing underexpansion ratios, $\dot{m}/\dot{m}_s$, tended to reduce effects of unsteadiness as represented by pressure fluctuations in the flow passage and reduced slugging of liquid below the passage exit seen on high-speed photographs of the flow. The penalty for the increased stability of the flow, however, is slower development of the multiphase jet, represented by higher levels of void fraction along the axis.

3. Use of the LHF and effective adapted-jet approximations yielded encouraging predictions of some properties of injection of air into water, particularly for large $\dot{m}/\dot{m}_s$ where effects of unsteadiness of the experiments were reduced. This included the evolution of time-averaged void fractions and the flow half-width based on time-averaged radial void fractions, as functions of distance from the passage exit. Deficiencies of the predictions were associated with the shape of the time-averaged void fraction profiles and underestimation of entrainment coefficients. General unsteadiness of the flow, for low values of $\dot{m}/\dot{m}_s$, and reverse shocks, for high values of $\dot{m}/\dot{m}_s$ are thought to be responsible for this behavior, since these phenomena tend to increase mixing rates in comparison to estimates based on steady flow. In contrast, failure of the LHF approximation does not offer an obvious explanation of the behavior, since this would cause predicted mixing rates to be higher than measured.

4. Air jets in liquids exhibit unusual flow widths, based on time-averaged void fractions, e.g. flow widths of ca. 0.3 in comparison to widths of 0.15 for typical single-phase jets. This behavior is due to the strong sensitivity of void fraction mixing levels.

REFERENCES

Abdel-Aal, H. K., Stiles, G. B. & Holland, C. C. 1966 Formation of interfacial area at high rates of gas flow through submerged orifices. AIChE J. 12, 174-180.

Addy, A. L. 1981 Effects of axisymmetric sonic nozzle geometry on Mach disk characteristics. AIAA J. 19, 121-122.

Avery, J. F. & Faeth, G. M. 1975 Combustion of a submerged gaseous oxidizer jet in a liquid metal. Fifteenth Symposium (International) on Combustion The Combustion Institute, Pittsburgh, 419-428.

Bakaklevskii, Y. I. & Chekhovich, V. Y. 1978 Temperature field of a submerged steam jet. J. Engr. Phys. 34, 329-333.

Bilger, R. W. 1976 Turbulent jet diffusion flames. Prog. Energy Combust. Sci. 1, 87-109.

Bogdanoff, D. W. 1983 Compressibility effects in turbulent shear layers. AIAA J. 21, 926-927.

Chan, C. K. 1974 Dynamical pressure pulse in steam jet condensation. Proc. Fifth Intl. Heat Trans. Conf. ASME, New York, 3, 226-230.

Chen, L.-D. & Faeth, G. M. 1982 Condensation of submerged vapor jets in subcooled liquids. J. Heat Trans. 104, 774-780.

Chen, L.-D. & Faeth, G. M. 1983 Structure of turbulent reacting gas jets submerged in liquid metals. Combust. Sci. Tech. 31, 277-296.

Chuech, S. G., Lai, M.-C. & Faeth, G. M. 1987 Structure of sonic underexpanded turbulent air jets in still air. Interim Report, Navy Contract No. N00014-85-K-0604, Dept. Aerospace Engr., The University of Michigan, Ann Arbor, MI.

Chuech, S. G., Lai, M.-C. & Faeth, G. M. 1988 Structure of turbulent sonic underexpanded free jets. AIAA Paper No. 88-0700.

Chun, J. H. & Sonin, A. A. 1984 Small-scale simulation of vapor discharges into subcooled liquid pools. National Heat Transfer Conference, Niagara Falls, NY.

Cumo, M., Farello, G. E. & Ferrari, G. 1978 Direct heat transfer in pressure-suppression systems. Proc. Sixth Intl. Heat Trans. Conf. ASME, New York, 5, 101-106.

Dash, S. M., Wolf, D. E. & Seiner, J. M. 1985 Analysis of turbulent underexpanded jets, part II: parabolized Navier-Stokes model, SCIPVIS. AIAA J. 23, 505-514.

Eggers, J. M. 1966 Velocity profiles and eddy viscosity distributions downstream of a Mach 2.2 nozzle exhausting to quiescent air. NASA TN D-3601.

Faeth, G. M. 1983 Evaporation and combustion of sprays. Prog. Energy Combust. Sci. 9, 1-76.

Hinze, J. O. 1975 Turbulence. Second Edition, McGraw-Hill, New York, pp. 286-300, 715-742.

Jeng, S.-M. & Faeth, G. M. 1984 Species concentrations and turbulence properties buoyant methane diffusion flames. J. Heat Trans. 106, 721-727.

Kerney, P. J., Faeth, G. M. & Olson, D. R. 1972 Penetration characteristics of a submerged steam jet. AIChE J. 18, 548-553.

Kudo, A., Egusa, T. & Toda, S. 1974 Basic study on vapor suppression. Proc. Fifth Intl. Heat Trans. Conf. ASME, New York, Vol. 3, 221-225.

Lambier, G. R. & Chow, L. C. 1984 Pressure pulses during vertical and horizontal discharges of steam into subcooled water. National Heat Transfer Conference, Niagara Falls, NY.

Lee, L., Bankoff, S. G., Yuen, M. C. & Tanking, R. S. 1979 Local condensation rate in horizontal co-current steam-water flow. 18th National Heat Transfer Conference, San Diego, CA.

Limbaugh, C. C. & Kneile, K. R. 1984 Uncertainties propagation for combustion diagnostics using infrared band models. J. Quant. Spec. Rad. Trans. 31, 161-171.

Lockwood, F. C. & Naguib, A. S. 1975 The prediction of the fluctuations in the properties of free, round jet, turbulent diffusion flames. Combust. Flame 24, 109-124.

Mahalingen, R., Limaye, R. S. & Brink, J. A., Jr. 1976 Velocity measurements in two-phase bubble-flow regime with laser-Doppler anemometry. AIChE J 22, 1152-1155.

Mao, C.-P., Szekely, G. A., Jr. & Faeth, G. M. 1980 Evaluation of a locally homogeneous flow model of spray combustion. J. Energy 4, 78-87.

Ohba, K., Kishimoto, I. & Ogasawara, M. 1977 Simultaneous measurements of local liquid velocity and void fraction in bubbly flows using a gas laser -- I. principles and measuring procedure. Tech. Rept. Osaka University 26, 547-556.

Ohba, K. 1979 Relationships between radiation transmissivity and void fraction in two-phase/dispersed flow. Tech. Rept. Osaka University 29, 245-254.

Papamoschou, D. & Roshko, A. 1986 Observations of supersonic free shear layers, AIAA Paper No. 86-0162.

Ricou, F. P. & Spalding, D. B. 1961 Measurements of entrainment by axisymmetricl turbulent jets. J. Fluid Mech. 11, 21-32.

Ruff, G. A., Sagar, A. D. & Faeth, G. M. 1988 Structure and mixing properties of pressure-atomized sprays. AIAA Paper No. 88-0237.

Santoro, R. J., Semerjian, H. R., Emmerman, P. J. & Goulard, R. 1981 Optical tomography for flow field diagnostics. Int. J. Heat Mass Trans. 24, 1139-1150.

Schlichting, H. 1979 Boundary Layer Theory. McGraw-Hill, New York, p. 599.

Schrock, V. E. 1969 Two-Phase Flow Instrumentation. ASME, New York, 24-35.

Seiner, J. M. & Norum, T. D. 1979 Experiments of shock associated noise and supersonic jets. AIAA Paper No. 79-1526.

Seiner, J. M. & Norum, T. D. 1980 Aerodynamic aspects of shock containing jet plumes. AIAA Paper No. 80-0965.

Shapiro, A. 1954 Compressible Fluid Flow, Vol. 1, Ronald Press, New York.

Shearer, A. J., Tamura, H. & Faeth, G. M. 1979 Evaluation of a locally homogeneous flow model of spray evaporation. J. of Energy 3, 271-278.

Shuen, J.-S., Solomon, A.S.P., Zhang, Q.-F. & Faeth, G. M. 1984 Structure of particle-laden jets: measurements and predictions. AIAA J. 23, 396-404.

Simpson, M. E. & Chan, C. K. 1982 Hydrodynamics of a subsonic vapor jet in a subcooled liquid. J. Heat Trans. 104, 271-278.

Soo, S. L. 1967 Fluid Dynamics of Multiphase Systems. Blaisdell Publishing Co., Waltham, MA.

Spalding, D. B. 1977 GENMIX: A General Computer Program for Two-Dimensional Parabolic Phenomena. Pergamon Press, Oxford.

Sun, T.-Y., Chuech, S. G., Parthasarathy, R. N. & Faeth, G. M. 1985 Turbulent noncondensing and condensing gas jets in liquids. Final Report, Navy Contract No. N00015-85-K-0148, Dept. of Mech. Engr., The Pennsylvania State University, University Park, PA.

Sun, T.-Y. & Faeth, G. M. 1986 Structure of turbulent bubbly jets - I. methods and centerline properties. Int. J. Multiphase Flow 12, 99-114; - II phase property profiles. Ibid., 115-126.

Sun, T.-Y., Parthasarathy, R. N. & Faeth, G. M. 1986 Structure of bubbly round condensing jets. J. Heat Trans. 108, 951-959.

Surin, V. A., Erchenko, V. N. & Rubin, V. M. 1983 Propagation of a gas jet in a liquid. J. Engr. Phys. 45, 1091-1101.

Tross, S. R. 1974 Characteristics of a turbulent two-phase submerged free jet. M.S. Thesis, The Pennsylvania State University, University Park, PA.

Wallis, G. 1969 One-Dimensional Two-Phase Flow. McGraw-Hill, New York.

Weimer, J. C., Faeth, G. M. & Olson, D. R. 1973 Penetration of vapor jets submerged in subcooled liquids. AIChE J. 19, 552-558.

Wygnanski, I. & Fiedler, H. 1969 Some measurements in the self-preserving jet. J. Fluid Mech. 38, 577-612.

Young, R. J., Yang, K. T. & Novotny, J. L. 1974 Vapor-liquid interaction in a high velocity vapor jet condensing in a coaxial water flow. Proc. Fifth Intl. Heat Trans. Conf. 3, ASME, New York, 226-230.

ONR REPORT DISTRIBUTION LIST: CLOSED, LIQUID METAL COMBUSTION*

Dr. Gabriel D. Roy (2)
Mechanics Division, Code 1132 P
Office of Naval Research
800 N. Quincy Street
Arlington, VA 22217-5000

Dr. Richard S. Miller (2)
Mechanics Division, Code 1132P
Office of Naval Research
800 N. Quincy Street
Arlington, VA 22217-5000

Dr. Lynn A. Parnell
Naval Ocean System Center
Code 6341
San Diego, CA 92152-5000

Defense Documentation Center (12)
Building 5, Cameron Station
Alexandria, VA 22314

Technical Information Division (6)
Naval Research Laboratory
4555 Overlook Avenue SW
Washington, DC 20375

Dr. Jerry A. Smith
Chemistry Division
Office of Naval Research
800 N. Quincy Street
Arlington, VA 22217

Dr. Albert D. Wood
Technology Programs
Office of Naval Research
800 N. Quincy St.
Arlington, VA 22217

Dr. H.W. Carhart
Combustion & Fuels
Naval REsearch Laboratory
Washington, DC 20375

Professor Allen Fuhs
Department of Aeronautics
Naval Post Graduate School
Monterey, CA 93943

Division Director
Engineering and Weapons
US Naval Academy
Annapolis, MD 21402

Mr. Francis J. Romano
Code 63R3
Naval Sea Systems Command
Washington, DC 20363

Mr. Norman D. Hubele
Fluidic Systems, MS 1301-RR
Garrett Pneumatic Systems Division
2801 East Washington St.
Phoenix, AZ 85034

Dr. Hugh H. Darsie
Advanced Technology Group
Substrand Energy Systems
4747 Harrison Avenue
Rockford, IL 61101

Dr. Daniel H. Kiely
Power & Energy Group
The Pennsylvania State University
Applied Research Laboratory
P.O. Box 30
State College, PA 16801

Professor Darryl E. Metzger
Department of Mechanical and
Aerospace Engineering
Arizona State University
Tempe, AZ 85281

Dr. Dae H. Cho
Reactor Analysis & Safety Division
Argonne National Laboratory
Argonne, IL 60439

Professor S.H. Chan
Department of Mechanical Engineering
The University of Wisconsin-Milwaukee
P.O. Box 784
Milwaukee, WI 53201

---

* One copy except as noted in parenthesis.

Professor George A. Brown
Department of Mechanical Engineering
and Applied Mechanics
University of Rhode Island
Kingston, RI 02881

Professor A. Murty Kanury
Department of Mechanical Engineering
Oregon State University
Corvallis, OR 97331

Professor Irvin Glassman
Department of Mechanical and
Aerospace Engineering
Engineering Quadrangle
Princeton University
Princeton, NY 08544

Professor Norman Chigier
Department of Mechanical Engineering
Carnegie-Mellon University
Pittsburgh, PA 15213

Professor George Janz
Cogswell Laboratory, R306
Department of Chemistry
Rensselaer Polytechnic Institute
Troy, NY 12181

Dr. Leonard Leibowitz
Chemical Technology Division
Argonne National Laboratory
9700 South Case Avenue
Argonne, IL 60439

Professor John Tarbell
104 Fenske Laboratory
Pennsylvania State University
University Park, PA 16801

Professor Thomas E. Daubert
104 Fenske Laboratory
Pennsylvania State University
University State Park, PA 16801

Dr. J. Braunstein
Research Division
Oak Ridge Operations
Department E
Oak Ridge, TN 37831

Mr. Robert Tompkins
Code 36621, Bldg. 126T
Naval Underwater Systems Center
Newport, RI 02841

Mr. Maurice F. Murphy
Code R33, Room 4-1711
Naval Surface Weapons, White Oak
Silver Spring, MD 20910

Dr. Kurt Mueller
Code R10
Energetic Materials Division
Naval Surface Weapons Center,
White Oak
Silver Spring, MD 20910

Dr. Earl Quandt, Jr.
Code 2704
David Taylor Naval Ship
Research and Development Center
Annapolis, MD 21402

Mr. Richard Bloomquist
Code 2752
David Taylor Naval Ship R&D Center
Annapolis, MD 21402

Dr. Lawrence P. Cook
High Temperature Processes Group
National Bureau of Standards
Washington, DC 20234

Dr. W. Lee
Research and Technology Department
Naval Surface Weapons Center
Silver Springs, MD 20703

END

DATE

FILMED

5-88

DTIC